Monthly Notices
of the
ROYAL ASTRONOMICAL SOCIETY

Mon. Not. R. Astron. Soc. **419,** 251–266 (2012) doi:10.1111/j.1365-2966.2011.19688.x

A 7 mm line survey of the shocked and disrupted molecular gas towards the W28 field TeV gamma-ray sources

B. P. Nicholas,[1⋆] G. Rowell,[1] M. G. Burton,[2] A. J. Walsh,[3] Y. Fukui,[4] A. Kawamura[4] and N. I. Maxted[1]

[1]*School of Chemistry and Physics, Adelaide University, Adelaide 5005, Australia*
[2]*School of Physics, University of New South Wales, Sydney 2052, Australia*
[3]*Centre for Astronomy, School of Engineering and Physical Sciences, James Cook University, Townsville 4811, Australia*
[4]*Department of Astrophysics, Nagoya University, Furocho, Chikusa-ku, Nagoya, Aichi 464-8602, Japan*

Accepted 2011 August 24. Received 2011 August 21; in original form 2011 May 28

ABSTRACT

We present 7 mm Mopra observations of the dense molecular gas towards the W28 supernova remnant (SNR) field, following a previous 12 mm line survey of this region. These observations take advantage of the 7 mm beam size to probe the dense and disrupted gas in the region at ∼1 arcmin scales. Our observations are focused towards the north-eastern (NE) HESS J1801−233 and southern HESS J1800−240 B TeV gamma-ray sources, with slightly less observations towards HESS J1800−240 A and C. Using the CS (1–0) transition we reveal multiple regions of dense gas, $n_{\rm H_2} \sim 10^5$ cm^{-3}. We report the discovery of dense gas towards HESS J1800−240 C, at the site of a 1720 MHz OH maser. The NE molecular cloud is known to be disrupted; many 1720 MHz OH masers and broad CO line emission are detected at the rim of W28. Here, we reveal this shock interaction region contains generally extended clumpy CS, as well as clumpy SiO and CH_3OH emission with broad line profiles. The full width at half maximum (FWHM) of the molecular lines extend up to 18 km s^{-1} on the W28 side of the NE cloud. The detection of SiO towards maser clumps OH C, D, E and F provides further evidence of the shocked conditions in the NE cloud. Several other lines associated with star formation are also detected towards the southern source, notably the energetic H II complex G5.89−0.39. The spatial match of dense gas with the TeV emission further supports the cosmic ray (CR) origin for the gamma-rays. We estimate the mass of several extended dense clouds within the field and predict the TeV flux from the dense cloud components. The predicted fluxes are of the order of 10^{-14} to 10^{-13} photons cm^{-2} s^{-1}, which should be detectable and possibly resolved by a future TeV instrument, such as the Cherenkov Telescope Array.

Key words: molecular data – supernovae: individual: W28 – ISM: clouds – H II regions – ISM: supernova remnants – gamma-rays: ISM.

1 INTRODUCTION

W28 is a striking example of TeV (10^{12} eV) gamma-ray emission spatially overlapping with molecular gas (Aharonian et al. 2008a). W28 is part of the increasing list of sources with spatial overlap between TeV or GeV (10^9 eV) gamma-ray emission and molecular gas [e.g. HESS J1745−290/SNR G359.1−0.5 (Aharonian et al. 2004), HESS J1714−385/CTB 37A (Aharonian et al. 2008b), HESS J1923+141/SNR G49.2−0.7 (Feinstein et al. 2009), IC 443 (Albert et al. 2008; Acciari et al. 2009)], in addition to the central molecular zone (CMZ) towards the Galactic Centre region (Aharonian et al. 2006).

W28 is a mixed morphology old age (>10^4 yr; Kaspi et al. 1993) supernova remnant (SNR) with dimensions of 50 arcmin × 45 arcmin. W28 is estimated to be at a distance of 1.2 to 3.3 kpc (e.g. Goudis 1976; Lozinskaya 1981; Motogi et al. 2011). It has been shown to exhibit non-thermal radio emission (Dubner et al. 2000), thermal X-ray emission (Rho & Borkowski 2002) and, more recently, gamma-ray emission at TeV (Aharonian et al. 2008a) and GeV (Abdo et al. 2010; Giuliani et al. 2010) energies.

Several CO surveys in the (1–0), (2–1) and (3–2) lines reveal massive molecular clouds (MCs) to the north-east (NE) and to the south (S) of the SNR (Arikawa et al. 1999; Torres et al. 2003; Reach, Rho & Jarrett 2005; Aharonian et al. 2008a; Fukui et al.

⋆E-mail: brent.nicholas@adelaide.edu.au

2008). Most of the CO emission appears centred at a local standard of rest velocity ($V_{\rm LSR}$) similar to that inferred for W28 $V_{\rm LSR} \sim 7\,{\rm km\,s^{-1}}$ (corresponding to a distance $\sim$2 kpc) based on H I studies (Velázquez et al. 2002).

The MCs NE of W28 are known to exhibit broad CO line emission. It has been argued that W28 has disrupted much of this gas, giving rise to its broad velocity distribution (Arikawa et al. 1999; Torres et al. 2003; Reach et al. 2005). The most likely mechanism for this type of disruption would be the SNR shock interacting with the molecular gas, as is the case for other sources, e.g. HESS J1745−290/SNR G359.1−0.5 (Aharonian et al. 2004), HESS J1714−385/CTB 37A (Aharonian et al. 2008b), HESS J1923+141/SNR G49.2−0.7 (Feinstein et al. 2009) and IC 443 (Albert et al. 2008; Acciari et al. 2009). All of these sources similarly display 1720 MHz OH masers and are mature SNRs (age $>10^4$ yr). Our NH_3 observations (Nicholas et al. 2011) revealed that the W28 SNR shock has disrupted the dense core of the NE cloud, and strong NH_3 (3,3) and (6,6) detections with broad linewidths [full width at half maximum (FWHM) $> 10\,{\rm km\,s^{-1}}$] suggest that this region is warm and turbulent. The shocked NE cloud also provides an opportunity to study the diffusion and propagation of CRs into MCs. Additionally, the effects of a SNR shock propagating through a dense MC can be studied and search for sites of star formation triggered by the passing shock.

The southern clouds harbour sites of high-mass star formation, containing multiple H II regions, G6.225−0.569, G6.1−0.6 (Lockman 1989; Kuchar & Clark 1997) and the ultracompact H II region (UCH II) G5.89−0.39, (see e.g. Harvey & Forveille 1988; Kim & Koo 2001). A recently detected 1720 MHz OH maser towards a candidate SNR G5.71−0.08 (Brogan et al. 2006) may also suggest that there is another SNR shock with molecular gas interaction occurring in one of the southern clouds. A key question is whether the W28 SNR has disrupted the southern clouds and is responsible for the TeV emission, or whether other high-energy processes are at play. The star formation activity present in the southern clouds may play a part in the production of TeV emission, as theory into protostellar particle acceleration may suggest (Araudo et al. 2007).

The TeV gamma-ray emission detected towards the NE cloud has strong evidence supporting the hadronic emission mechanism. In order to model leptonic scenarios, uncomfortably low magnetic fields and gas densities are required (Yamazaki et al. 2006; Fujita et al. 2009; Abdo et al. 2010; Gabici et al. 2010). These requirements contradict with the observed molecular gas densities $n_{\rm H_2} > 10^4\,{\rm cm^{-3}}$ (Nicholas et al. 2011) and the magnetic field enhancements seen in dense MCs (Crutcher 1991). The key question relates to the origin of the TeV particles. Provided the hadronic emission scenario, a population of high-energy particles are required to interact with the dense clouds. For the NE cloud, the SNR shock is the obvious source of accelerated particles. However, the same cannot be conclusively said about the southern sources. CRs accelerated by W28 in the past may have propagated south to illuminate the southern clouds. Additionally, multiple H II regions and sites of star formation, including the energetic UCH II complex G5.89−0.39, could assist in CR acceleration towards the southern TeV sources.

Since the common and abundant gas tracer, CO, with a critical density of $10^2\,{\rm cm^{-3}}$, rapidly becomes optically thick towards clumps and cores, probing the MC density profile can be impaired. Ideal tracers of dense gas are those with a lower abundance ($10^{-5}\times$ CO) and higher critical density (10^4–$10^5\,{\rm cm^{-3}}$). Using the Mopra telescope, we (Nicholas et al. 2011) conducted broad scale ($\sim$1.5 deg^2) observations of the W28 field in a 12 mm line survey. Taking advantage of the 23 GHz NH_3 inversion lines, the cold dense interiors of the MCs were probed and revealed dense gas spatially consistent with both the CO gas and TeV emission.

In order to further probe the structure and details of the W28 field MCs, we have continued to use the Mopra radio telescope in a 7 mm line survey to observe the CS (1–0) line, as well as other lines including SiO (1–0), Class I CH_3OH masers and cyanopolyynes HC_nN ($n = 3, 5, 7$), to trace the dense gas, the presence of shocks, outflows, and disrupted gas, and sites of high-mass star formation.

The 43 GHz CS (1–0) line is a useful warm, dense gas tracer, and, as CS also exists in various isotopologue forms, the optical depth and column density can be constrained. The higher frequency of 7 mm lines compared to our previous 12 mm observations results in a smaller beam FWHM ($\sim$1 arcmin). This makes CS an ideal follow-up tracer to determine the properties of the dense and disrupted gas towards the MCs in the W28 region.

2 MOPRA OBSERVATIONS AND DATA REDUCTION

Observations were performed with the Mopra radio telescope in 2009 April and 2010 March and utilized the University of New South Wales (UNSW) Mopra wide-band spectrometer (MOPS) in zoom mode. Mopra is a 22-m single-dish radio telescope located $\sim$450 km north-west (NW) of Sydney, Australia (31°16′04″ S, 149°05′59″ E, 866 m a.s.l.). The 7 mm receiver operates in the 30–50 GHz range and, when coupled with MOPS, allows an instantaneous 8 GHz bandwidth. This gives Mopra the ability to cover 40 per cent of the 7 mm band and simultaneously observe many spectral lines. The zoom mode of MOPS allows observations in up to 16 windows simultaneously, where each window is 137.5 MHz wide and contains 4096 channels in each of two polarizations. At 7 mm this gives MOPS an effective bandwidth of $\sim$1000 km s^{-1} with resolution of $\sim$0.2 km s^{-1}. Across the whole 7 mm band, the beam FWHM varies from 1.37 (31 GHz) to 0.99 arcmin (49 GHz) (Urquhart et al. 2010). Table 1 lists the lines which MOPS was tuned to receive.

'On-the-fly' (OTF) mapping observations were based on our earlier 12 mm mapping of the W28 region. Although we mapped all four TeV sources, deeper observations towards the NE shocked cloud (HESS J1801−233) and southern cloud (HESS

Table 1. Molecular lines and their corresponding rest frequencies which MOPS was tuned to receive. The final two columns indicate whether the line was detected in our mapping or deep pointing observations.

Molecular line name	Frequency (MHz)	Detected map	Detected deep spectra
^{30}SiO (1–0, $v = 0$)	42 373.365	–	–
SiO (1–0, $v = 3$)	42 519.373	Yes	–
SiO (1–0, $v = 2$)	42 820.582	Yes	–
^{29}SiO (1–0, $v = 0$)	42 879.922	–	–
SiO (1–0, $v = 1$)	43 122.079	Yes	–
SiO (1–0, $v = 0$)	43 423.864	Yes	Yes
CH_3OH-I	44 069.476	Yes	Yes
HC_7N (40–39)	45 119.064	–	–
HC_5N (17–16)	45 264.75	Yes	Yes
HC_3N (5–4)	45 488.839	Yes	Yes
^{13}CS (1–0)	46 247.58	Yes	Yes
HC_5N (16–15)	47 927.275	Yes	Yes
C^{34}S (1–0)	48 206.946	Yes	Yes
OCS (4–3)	48 651.6043	–	–
CS (1–0)	48 990.957	Yes	Yes

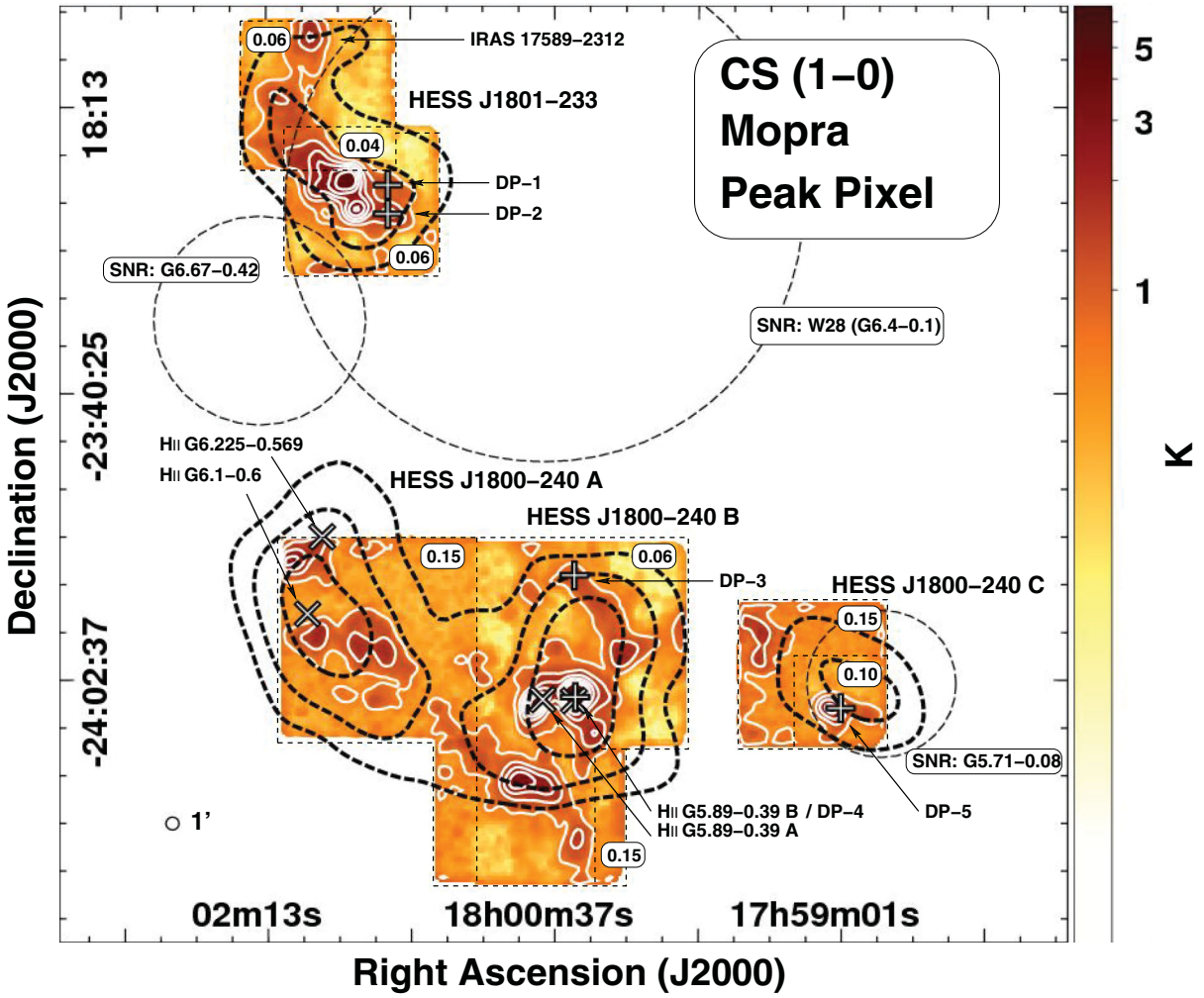

Figure 1. CS (1–0) peak pixel map of the W28 region (log scale image with white linear contours, minimum contour $\sim 10\,T_{\rm RMS}$) with black/white crosses + to indicate the locations of the position-switched deep pointings (DP-1 to DP-5). Thick black dashed contours are the HESS TeV emission (4σ, 5σ, 6σ levels) revealing HESS J1801−233 and the different components of HESS J1800−240. Boundaries of catalogued SNRs are indicated by dashed circles, and locations of H II regions are indicated by black/white crosses ×. Black dashed boxes are used to separate regions based on their exposure. The numbers presented in the white boxes are the mean main beam $T_{\rm RMS}$ (units of K) achieved across the 42–49 GHz band within that boundary. The 1 arcmin beam FWHM is also shown in the lower-left corner.

J1800−240 B) were obtained than towards HESS J1800−240 A & C. The observations were recorded alternating the scanning direction from RA to Dec. to reduce noise levels and to eliminate artificial stripes that can be introduced when only one scanning direction is used. Collectively, over both observation runs we obtained nine passes on the NE cloud (HESS J1801−233), nine passes towards the southern cloud (HESS J1800−240 B) and three passes towards each of the HESS J1800−240 A and HESS J1800−240 C regions.

Data were reduced using the standard Australia Telescope National Facility (ATNF) packages LIVEDATA, GRIDZILLA, ASAP and MIRIAD.[1] For mapping data, LIVEDATA was used to perform a bandpass calibration for each row using the preceding off-scan as a reference, and applied a linear fit to the baseline. GRIDZILLA re-gridded and combined all data from all mapping scans into a single data cube, with pixels $(\Delta x, \Delta y, \Delta z) = (15\ \text{arcsec}, 15\ \text{arcsec}, 0.21\ \text{km s}^{-1})$. The mapping data were also weighted according to the relevant $T_{\rm SYS}$, Gaussian-smoothed based on the Mopra beam (1.2 arcmin FWHM and 3 arcmin cut-off radius), and pixel masked to remove noisy edge pixels. Data cubes were then converted into an ASAP scantable and had a seventh-order polynomial function fit subtracted from each pixel in the cube before returning the final output fits files. The analysis of position-switched deep pointings employed ASAP with time-averaging, weighting by the relevant $T_{\rm SYS}$, and baseline subtraction using a linear fit after masking the 15 channels at each bandpass edge. Line parameters from a Gaussian fit to the spectra for all lines detected in the deep pointings are presented in the Appendix, Table A1.

In both mapping and position-switched data, the antenna temperature $T_{\rm A}^{*}$ (corrected for atmospheric attenuation and rearward loss) was converted to the main beam brightness temperature $T_{\rm mb}$ (K), such that $T_{\rm mb} = T_{\rm A}^{*}/\eta_{\rm mb}$ where $\eta_{\rm mb}$ is the Mopra main beam efficiency. Each line was corrected by the relevant $\eta_{\rm mb}$ following Urquhart et al. (2010).

Due to the uneven mapping exposure across the W28 field, the rms error in $T_{\rm mb}$, $T_{\rm RMS}$ (K), varies. On top of the exposure

[1] See http://www.atnf.csiro.au/computing/software/ for more information on these data reduction packages.

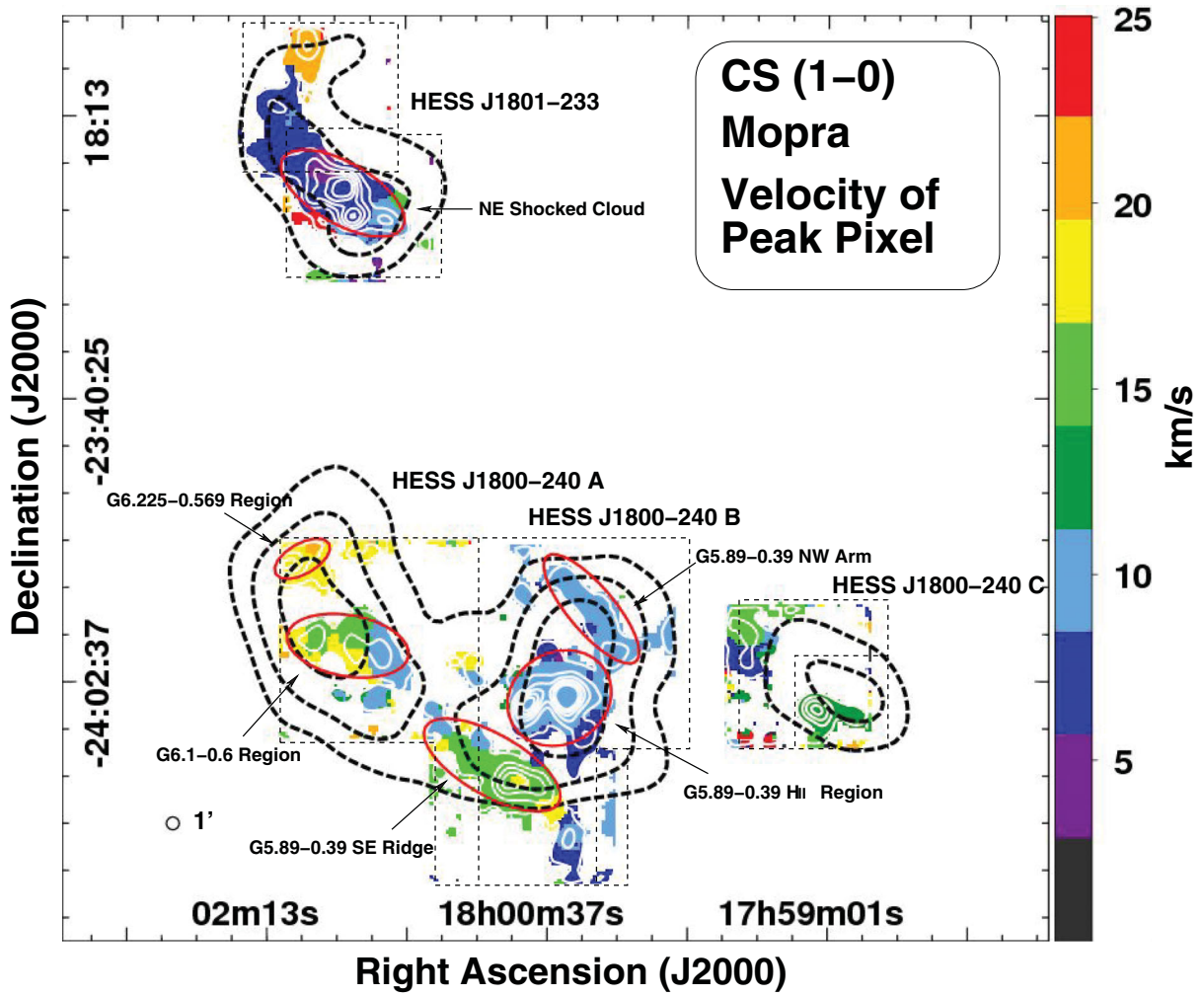

Figure 2. Velocity of the peak pixels, with the same black and white contours as shown in Fig. 1. Red solid ellipses are the regions where spectra were averaged in order to extract gas parameters as an extended source.

dependence, there is also a frequency dependence on $T_{\rm RMS}$ across the 42–49 GHz band. For this reason in Fig. 1 we present a CS (1–0) peak pixel map of the W28 field with dashed boxes outlining the exposure boundaries. The numbers presented in the white boxes are the averaged $T_{\rm RMS}$ achieved (across the 42–49 GHz band) within that boundary. We also show in Fig. 2 the velocity of the peak pixels to show the general velocity locations and distribution of the various clumps of CS (1–0) gas. We show the same contours in both Figs 1 and 2 for guidance.

For the detected lines, images of velocity-integrated intensity, position velocity (PV) and velocity dispersion ($v_{\rm RMS}$) have been produced where possible (although not all are shown). Velocity-integrated intensity images (MIRIAD 0th moment) are integrated over a velocity range determined by the observed linewidth. This was chosen to encompass the bulk of the emission from the region of interest. Minimum contour levels were set based on the integrated $T_{\rm RMS}$ of the emission. The integrated $T_{\rm RMS}$ of each image was determined by creating additional MIRIAD 0th moment maps in a velocity space either side of the velocity range of interest, ensuring the same number of channels were used. These additional moment maps were used to create pixel distribution histograms which were Gaussian fitted. In this way we estimated the integrated $T_{\rm RMS}$ from the Gaussian fit results. On all images, the minimum contour levels are mentioned in terms of the raw value as well as $T_{\rm RMS}$. Generally, the minimum accepted contour level on integrated maps is $2\,T_{\rm RMS}$. PV plots were created by re-ordering the data cubes axes and Hanning smoothing the velocity axis (width $\sim$3 km s^{-1}) to improve image quality. The PV plots show the peak pixel along the declination axis for illustrative purposes. Intensity weighted velocity dispersion (MIRIAD 2 moment), $v_{\rm RMS}$, maps were calculated for pixels above a reasonable threshold.

3 ANALYSIS AND RESULTS OVERVIEW

Of the 17 molecular transitions searched for (Table 1), 11 were detected. From the mapping data we detected: CS, $C^{34}S$ and ^{13}CS in the (1–0) transition; SiO (1–0) in several vibrational modes; CH_3OH; HC_3N (5–4) and HC_5N in the (17–16) and (16–15) transitions.

3.1 CS emission

The CS (1–0) line was detected across the W28 field and is the most prominent. Along with the common CS isotopologue, $^{12}C^{32}S$, we also detect other isotopologues, $C^{34}S$ and ^{13}CS in the (1–0) transition. Unless otherwise indicated, CS refers to the common $^{12}C^{32}S$ isotopologue. From our deep pointing observations (DP-1 to DP-5, locations shown in Fig. 1) with $T_{\rm RMS} \sim 2$ times lower than the mapping data, a Gaussian fit to the detected isotopologue

Table 2. Calculated gas parameters from CS (1–0), $C^{34}S$ (1–0) and ^{13}CS (1–0) isotopologue ratios from deep pointing observations DP-1 to DP-5 (Fig. 1). Columns from left to right are: region name, CS (1–0) peak T_{mb} temperature, CS (1–0) LSR velocity, CS (1–0) FWHM, CS (1–0) optical depth τ, assumed kinetic temperature T_k, beam corrected total column density N[CS], hydrogen column density $N[H_2]$, mass, molecular hydrogen number density n_{H_2} and virial mass range M_{vir}. The virial mass range is the lower and upper bounds when considering a constant, Gaussian and r^{-2} density profile.

Core / region	T_{mb} (K)	V_{LSR} (km s^{-1})	FWHM (km s^{-1})	τ	T_k [a] (K)	N[CS] ($\times 10^{14}$ cm^{-2})	$N[H_2]$ ($\times 10^{23}$ cm^{-2})	Mass ($M_\odot$)	n_{H_2} ($\times 10^5$ cm^{-3})	Virial mass ($\times 10^2 M_\odot$)
					– Compact source –					
DP-1	1.1	13.1	18.1	1.0	46	16.5	4.1	790	6.9	133–279
DP-2	2.4	7.4	11.2	1.6	46	28.8	7.2	1400	12.0	23–81
DP-3[b]	1.4	9.0	2.2	–	20	0.1	2.2×10^{-2}	77	0.5	1.2–4.3
DP-4	9.5	9.3	4.0	2.8	33	61.1	15.3	2900	25.4	3.4–11.9
DP-5[c]	2.8	13.0	1.1	2.1	20	4.0	1.0	190	1.7	0.3–0.9
Compact-source mass/density scaling factors versus radius R (pc)										
R (pc)			0.10 0.15 0.20 0.25 0.30 0.35 0.40							
Mass $M(R)/M(0.2\,pc)$			0.89 0.93 1.00 1.09 0.21 1.36 1.54							
Density $n_{H_2}(R)/n_{H_2}(0.2\,pc)$			7.09 2.21 1.00 0.56 0.36 0.25 0.19							

[a] Temperatures from NH_3 observations (Nicholas et al. 2011).
[b] Using only CS (1–0) and assuming optically thin emission.
[c] Using only CS (1–0) and $C^{34}S$ (1–0).

Table 3. Calculated gas parameters from CS (1–0), $C^{34}S$ (1–0) and ^{13}CS (1–0) isotopologue ratios for extended sources, using averaged spectra from mapping observations. Columns from left to right are: region name, peak T_{mb} temperature, CS (1–0) line FWHM, optical depth τ, assumed kinetic temperature T_k, beam corrected total column density N[CS], hydrogen column density $N[H_2]$, mass and molecular hydrogen number density n_{H_2}. We treat the NE shocked cloud mass as an upper limit resulting from uncertainties in the molecular abundance ratio.

Region	T_{mb} (K)	FWHM (km s^{-1})	τ*	T_k † (K)	N[CS] ($\times 10^{14}$ cm^{-2})	$N[H_2]$ ($\times 10^{23}$ cm^{-2})	Mass ($M_\odot$)	n_{H_2} ($\times 10^4$ cm^{-3})
				– Extended source –				
NE shocked cloud[a]	1.8	7.3	2.3	35	17.8	4.4	<56000	6.1
G5.89−0.39 H II region[b]	2.2	3.8	3.8	25	11.6	2.9	54000	2.7
G5.89−0.39 NW arm[c]	0.8	3.5	–	20	1.4	0.3	4200	0.6
G5.89−0.39 SE ridge[d]	0.7	3.1	–	16	2.7	0.7	12000	0.9
G6.1−0.6 region[e]	0.7	5.1	–	25	1.8	0.5	6500	0.6
G6.225−0.569 region[f]	1.5	3.4	–	21	1.8	0.5	1600	1.2

* Optical depths are calculated where possible; if no number is given then the emission is assumed to be optically thin.
† Temperatures from NH_3 observations (Nicholas et al. 2011).
[a] For ellipse 7.2 × 2.8 pc diam.; pos. angle −30°; centred on RA 18:01:46.7 Dec. −23:24:21.9 shown in Fig. 2.
[b] For ellipse 4.8 × 4.2 pc diam.; pos. angle +30°; centred on RA 18:00:32.9 Dec. −24:03:59.2 shown in Fig. 2.
[c] For ellipse 6.3 × 2.1 pc diam.; pos. angle −50°; centred on RA 18:00:22.0 Dec. −23:56:59.2 shown in Fig. 2.
[d] For ellipse 7.0 × 2.8 pc diam.; pos. angle −30°; centred on RA 18:00:55.9 Dec. −24:09:14.1 shown in Fig. 2.
[e] For ellipse 5.6 × 2.8 pc diam.; pos. angle −10°; centred on RA 18:01:45.2 Dec. −23:59:51.2 shown in Fig. 2.
[f] For ellipse 2.8 × 1.4 pc diam.; pos. angle +30°; centred on RA 18:02:00.7 Dec. −23:53:01.4 shown in Fig. 2.

line emission allowed the optical depth and column density to be estimated. The method assumed an elemental abundance ratio between CS and the rarer isotopologues of 22.5 for [CS]/[$C^{34}S$] and 75 for [CS]/[^{13}CS] to calculate the optical depth using Zinchenko et al. (1994, equation 1). The upper state column density was then estimated via the method from Goldsmith & Langer (1999, equation 9). The total column density of all states was obtained by applying a local thermal equilibrium (LTE) approximation and using temperature estimations from our NH_3 observations (Nicholas et al. 2011), assuming that the CS gas is tracing the same gas as our NH_3 observations. From these parameters, the LTE hydrogen mass, number density and virial mass were estimated via the methods outlined in Nicholas et al. (2011), by assuming a compact-source size r = 0.2 pc and a molecular abundance ratio, χ_{CS}, of CS to H_2. CS molecular abundance ratios are known to vary dramatically from different sites in the Galaxy, ranging from 1×10^{-8} (Frerking, Wilson & Linke 1980, e.g. Sgr B – Table 4) to 6×10^{-11} (Linke & Goldsmith 1980, e.g. W43 – Table 3). We adopted an abundance ratio of $\chi_{CS} = 4 \times 10^{-9}$ (Irvine, Goldsmith & Hjalmarson 1987) following Zinchenko et al. (1994) which is typical for dense quiescent gas. This is likely the case for most of the clumps, with the exception of the NE cloud as later discussed in Section 5.1. The results of our compact-source size LTE analysis and cloud mass/densities from deep pointing observations are displayed in Table 2.

The LTE analysis method has also been applied to larger extended regions by utilizing spectra from mapping data. For extended source calculations, we extracted and averaged the spectra for all pixels contained within an elliptical region. In this way, we apply the standard analysis outlined above to single averaged spectra for the entire region. We used the same abundance ratio, but assumed the emission fills a volume defined by a prolate ellipsoid of volume $V = 4/3 \times \pi\, r_1\, r_2^2$. Results of the extended source LTE analysis from mapping data are displayed in Table 3.

3.2 SiO emission

We also tuned MOPS to include several different SiO (1–0) transitions arising from different vibrational modes (v = 0, 1, 2, 3),

as well as the isotopologues ^{29}SiO and ^{30}SiO. The SiO molecule is a known and proven signpost for the presence of shocked and disrupted gas (Schilke et al. 1997; Gusdorf et al. 2008a,b; Martin-Pintado et al. 2000). Our detection of SiO from several locations provides some insight into the disruptive conditions within the MCs. Unless otherwise indicated, SiO refers to ^{28}SiO in the $v = 0$ mode.

3.3 CH_3OH emission

Multiple detections of CH_3OH masers towards the southern clouds are indicative of the star formation activity present towards the H II regions and surrounding environments. Additional detections of CH_3OH emission in the NE cloud is interesting. To date, no star formation tracers such as: H_2O masers, CH_3OH masers or infrared emission have been detected towards this cloud. The CH_3OH emission in the NE cloud does not appear to correspond to stellar activity, as discussed later.

3.4 Cyanopolyyne HC_nN ($n = 3, 5, 7$) emission

Detections of the cyanopolyynes HC_3N (5–4), HC_5N (16–15) and HC_5N (17–16) towards the southern clouds are indicative of the activity in cold dense cores at the very early stages of high-mass star formation. Interestingly, additional detections of HC_3N (5–4) towards the shocked NE cloud are revealed. The sites of HC_3N (5–4) emission in the NE cloud do not appear to correspond to stellar activity.

A more detailed discussion of the morphology and implications of the molecular transitions detected from each of the mapped regions follows in Section 4.

4 SPECIFIC DISCUSSION OF REGIONS

4.1 North-eastern cloud/HESS J1801−233

Located at the northern boundary of HESS J1801−233 and nearby the giant H II region M20, we observe several molecular lines, which reveal dense gas and star formation activity. These molecular lines are all at a V_{LSR} range $\sim$20 km s^{-1}, which is further away than the rest of the molecular emission seen in the NE cloud, V_{LSR} $\sim$10 km s^{-1}, discussed later. This core was detected in our 12 mm study, where it was referred to as Core 1. Towards this northern most core is an *IRAS* source, IRAS 17589−2312 (Bronfman, Nyman & May 1996), and we adopt the *IRAS* nomenclature. The dense CS core seen here is likely part of a molecular bridge connecting down towards the peak of the HESS J1801−233 TeV emission seen in Fig. 1. We note that in the peak pixel map, Fig. 1, the lowest contour level is $\sim 10\,T_{RMS}$. This gives an indication to the prominence and the extent of the CS (1–0) emission detected towards the NE cloud and the W28 clouds in general. Towards IRAS 17589−2312, we observe multiple Class I CH_3OH masers along the line of sight within the beam. The maser emission is relatively weak (peak $T_{mb} \sim 0.6$ K) compared to the other CH_3OH masers seen in the W28 field discussed later. This detection adds to the list of maser transitions which have been observed from this region: 6.7 GHz CH_3OH (Fontani, Cesaroni & Furuya 2010), 22 GHz H_2O (Codella et al. 1995; Nicholas et al. 2011) and now 44 GHz CH_3OH.

We also detect the cyanopolyyne HC_3N (5–4) line towards this core indicating hot gas phase chemistry probably driven by the central source. There is also a detection of SiO (1–0) which indicates shocks and/or outflows originating from IRAS 17589−2312. Lefloch, Cernicharo & Pardo (2008) label this core as TC5 and suggest that the star formation in this core is recent and could possibly have been triggered by the W28 SNR. Spectra for the line emission detected towards this core are shown in Fig. A1 (in the online version of the journal – see Supporting Information).

Further south an extended dense region is spatially consistent with the TeV gamma-ray source HESS J1801−233. Towards the NE rim of W28 several mm-line surveys (Wootten 1981; Arikawa et al. 1999; Torres et al. 2003; Reach et al. 2005; Aharonian et al. 2008a; Fukui et al. 2008; Nicholas et al. 2011) have revealed the well-known SNR shock interaction site, traced by broad line measurements and the presence of many 1720 MHz OH masers (Frail, Goss & Slysh 1994; Claussen et al. 1997).

Fig. 3 contains integrated intensity images for emission detected towards this region. The CS (1–0) emission is spatially matched to the CO (2–1) emission measured by the Nanten telescope (Fukui et al. 2008), and NH_3 emission measured by Mopra revealed a dense clump in the NE cloud (Nicholas et al. 2011). This spatial overlap is generally expected as CS will trace the denser ($n \sim 10^5$ cm^{-3}) regions of the MCs. An image showing the spatial relationship between the CO (2–1), CS (1–0) and NH_3 (3,3) gas in the NE cloud is shown in Fig. A3 (in the online version of the journal – see Supporting Information).

The arcmin beam size allows the dense portion of the cloud to be probed in more detail than in our 2 arcmin beam NH_3 study. Fig. 3 highlights the clumpy nature of the cloud. Several dense clumps are arranged in a NE to south-west direction. We also note the minimum contour level for the integrated CS (1–0) emission in Fig. 3 is set to $10\,T_{RMS}$. The CS (1–0) emission is very prominent throughout the NE cloud and likely extends towards the limits of our mapping.

The line profiles of the CS and isotopologue emission are broad, with FWHM $\sim$ 18 km s^{-1} consistent with other molecular line observations from the region. Additionally, the asymmetry in the spectra provides evidence for the presence of shocks and gas disruption (Seta et al. 1998). Some CS line profiles indicate wings on the 'positive', or far side of the peak emission [e.g. CS (1–0) point 3/DP-1 in Fig. 3] and also on the 'negative', or nearer, side of the peak emission in others [e.g. CS (1–0) point 1/DP-2 in Fig. 3]. In addition to the asymmetric line profiles, symmetric line profiles (or at least profiles with similar wings on both sides of the peak emission) are also seen towards this NE cloud [e.g. CS (1–0) point 2 in Fig. 3]. These line profiles may suggest there are components of the shock travelling in different directions, the possibility of reverse shocks or may simply be a projection effect.

Several clumps of SiO (1–0) are detected and bounded by an arc of 1720 MHz OH masers, further confirming that a shock has disrupted this MC. The peak of the SiO (1–0) emission (point 15 in Fig. 3) lies offset from the peak of the dense gas traced by CS (1–0) (point 2 in Fig. 3), which may suggest that the densest CS (1–0) core is shielded from the disruption of the shock.

A Class I CH_3OH maser transition is detected towards the eastern edge of the dense gas (point 13 in Fig. 3). This is the weakest of the CH_3OH masers detected, with a peak temperature of $\sim$0.4 K. A second possible site of emission appears real from the DP-2 spectra (point 14/DP-2 in Fig. 3). Here the spectra are weak, peak $T_{mb} = 0.06$ K, but with broad FWHM = 15 km s^{-1}. Both these CH_3OH emission regions are not associated with typical star-forming cores. Rather, they appear to be a by-product of the SNR shock heating the gas in a similar manner as discussed, for the case of expanding shocks from H II regions in Voronkov et al. (2010). Similarly, the detection of HC_3N (5–4) from this region further indicates hot core gas phase chemistry. The emission is again broad, FWHM $\sim$12 km s^{-1} as for other lines detected from the region.

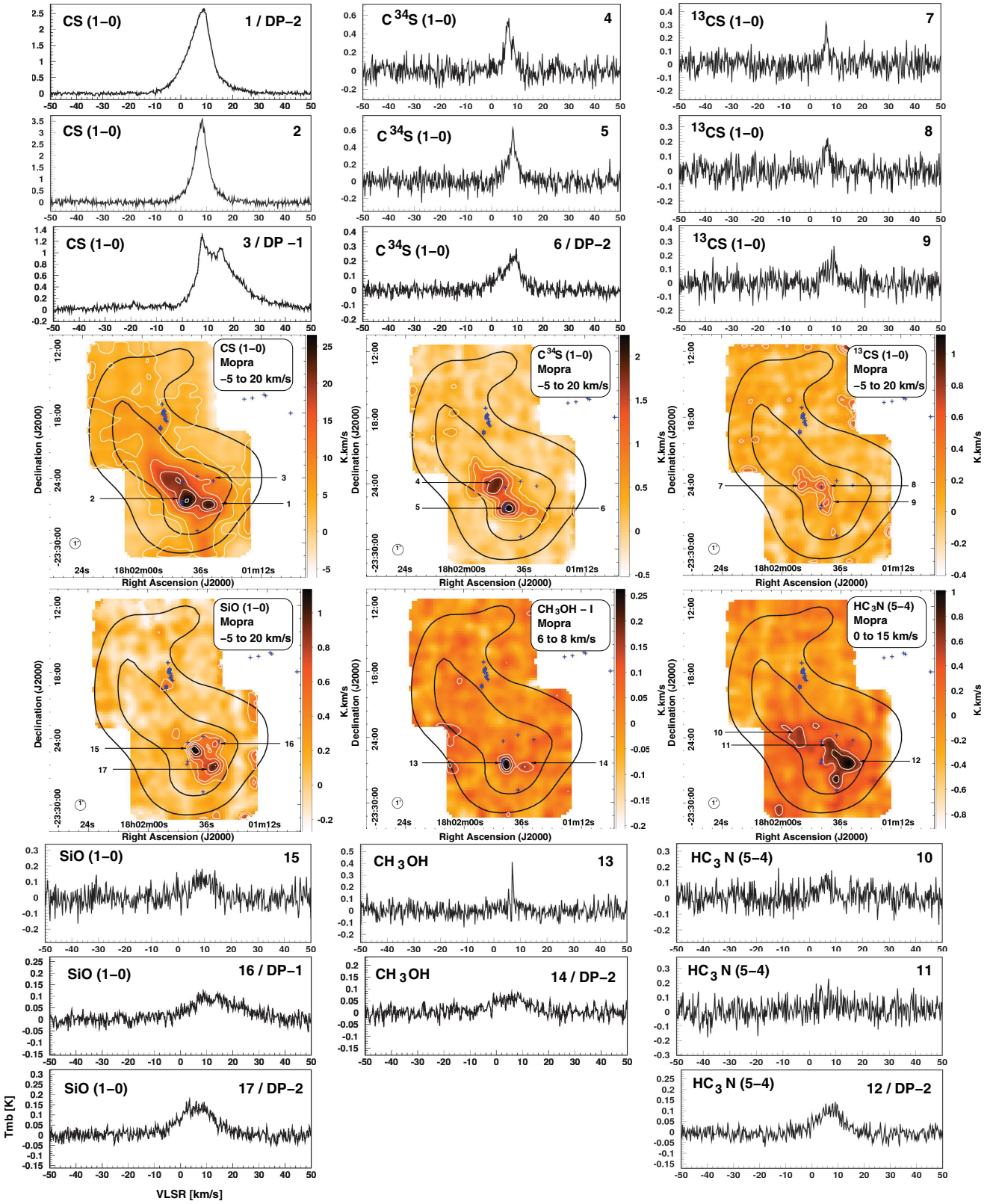

Figure 3. Integrated intensity images and spectra for the NE HESS J1801−233 region. Integration ranges are indicated on each panel. In all panels, HESS TeV emission is indicated by thick black contours (4 and 5σ levels), the positions of 1720 MHz OH masers from Claussen et al. (1997) are indicated by blue crosses +, and white contours are used to highlight the molecular emission from the image. Minimum contour level for: CS (1–0) is 2.6 K km s^{-1} ($\sim$10 $T_{\rm RMS}$), for C^{34}S (1–0) is 0.4 K km s^{-1} ($\sim$2 $T_{\rm RMS}$), for ^{13}CS (1–0) is 0.24 K km s^{-1} ($\sim$2 $T_{\rm RMS}$), for SiO (1–0) is 0.32 K km s^{-1} ($\sim$2 $T_{\rm RMS}$), for CH_3OH is 0.1 K km s^{-1} ($\sim$2 $T_{\rm RMS}$) and for HC_3N (5–4) is 0.5 K km s^{-1} ($\sim$2 $T_{\rm RMS}$). Surrounding the integrated intensity images are spectra taken from both the mapping data and deep pointings, labelled according to their locations.

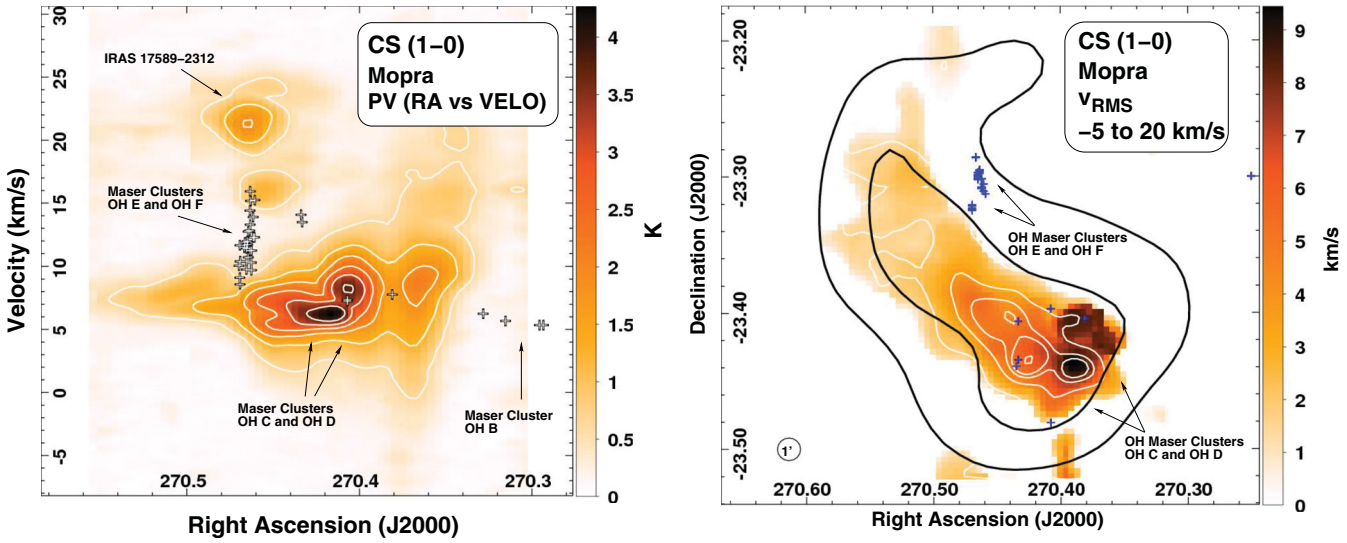

Figure 4. Left: PV plot for the NE region CS (1–0) emission. This RA versus V_{LSR} image is showing the peak pixel along the declination axis. Black/white crosses + represent the positions of the 1720 MHz OH masers with their corresponding labels from Claussen et al. (1997). The separate core at $V_{LSR} \sim 20\,km\,s^{-1}$ corresponds to the *IRAS* source. Right: velocity dispersion v_{RMS} map for the CS (1–0) emission from the NE region. The v_{RMS} has been calculated for emission $\geq$0.5 K in the -5 to $20\,km\,s^{-1}$ interval and then scaled to show the line FWHM. White contours are the integrated CS contours seen in Fig. 3. In both panels the RA axis is shown in degrees for clarity.

The PV plot shown in Fig. 4 highlights the CS (1–0) emission, especially from the western or W28 side of the dense cloud. The velocity at the peak pixel map shown in Fig. 2 reveals the existence of a velocity gradient, where the peak emission towards the south-western edge of the cloud has larger V_{LSR} values which decrease towards the NE. This gradient would suggest that the shock is disrupting the cloud from the south-western or W28 side. The velocity dispersion v_{RMS} image for the CS (1–0) emission (for $T_{mb} > 0.5$ K in the -5 to $20\,km\,s^{-1}$ range) from the NE region is also shown in Fig. 4. The emission with the largest v_{RMS} dispersion originates from the south-western side of the cloud, which was also the case for NH_3 (3,3) emission in Nicholas et al. (2011). The more disrupted emission is generally offset from the peaks seen in the integrated map, which are also shown in the PV plot (Fig. 4) as white contours. Interestingly one of the clumps seen in the CS(1–0) integrated map (point 1/DP-2 in Fig. 3) appears disrupted and has a large v_{RMS} value. This clump also corresponds to a peak in the SiO (1–0) integrated emission (point 17/DP-2 in Fig. 3).

We have taken two position switched deep pointings towards the NE cloud, specifically targeted towards the western side of the cloud where the most turbulent conditions are seen. The locations of the position switched observations are illustrated in Fig. 1. DP-1 is towards the broadest and most disruptive region, and DP-2 is towards a disrupted core. From these deep spectra, we have been able to extract gas parameters, which are displayed in Table 2. We find that the compact-source size mass, assuming a core with radius $r = 0.2$ pc, is more than a factor of 10 smaller than the mass obtained when using the virial theorem. This is to be expected as these observations are targeted to the most disrupted regions of the cloud which are not expected to be gravitationally bound. Additionally, the molecular abundance ratio may be quite different in this shocked region compared to the unshocked gas.

4.2 South-eastern cloud/HESS J1800−240 A

The region associated with HESS J1800−240 A contains two H II regions, G6.225−0.569 and G6.1−0.6 (Lockman 1989; Kuchar & Clark 1997) and IRAS 17588−2358. Integrated intensity maps of detected emission are shown in Fig. 5. Dense gas traced by CS (1–0) populates this region in clumpy cores near the two H II regions. A core unrelated to the H II regions (point 3 in Fig. 5) shows signs of extension and also displays a double peaked line profile towards its edge (point 4 in Fig. 5). Further south, additional clumps are detected with >5 integrated T_{RMS}. The line profiles of the CS emission towards these cores are also moderately broad, FWHM $\sim 5\,km\,s^{-1}$, but not to the extent of the emission seen in the NE cloud.

In the NE corner of our mapping, near the H II region 6.225−0.569, we trace star formation activity, detecting a bright Class I CH_3OH maser (peak $T_{mb} \sim 18$ K), a HC_3N (5–4) emitting core and evidence of shocks/outflows with a detection of SiO(1–0). The location of these star formation tracers is offset from the catalogued position of G6.225−0.569.

We note that this region, associated with HESS J1800−240 A, has less exposure (a factor of 3 lower than the NE HESS J1801−233 and southern HESS J1800−240 B regions).

4.3 Southern cloud/HESS J1800−240 B/G5.89−0.39

Spatially well matched to HESS J1800−240 B are three dense cores oriented in a south-east (SE) to NW alignment (points 1, 2 and 3 in Fig. 6), which were seen in our previous 12 mm observations (Nicholas et al. 2011, labelled as Triple Core SE, Central and NW). The SE and central sources are associated with the IR-bright and energetic UC H II region G5.89−0.39 and the NW source with a pulsating M-type star, V5561 Sgr, a further 5 arcmin away.

The extraordinary molecular outflow emanating from the H II complex G5.89−0.39 has been extensively studied from arcsec to arcmin scales in multiple molecular lines (e.g. Harvey & Forveille 1988; Churchwell, Walmsley & Cesaroni 1990; Zijlstra et al. 1990; Gomez et al. 1991; Choi, Evans & Jaffe 1993; Acord, Walmsley & Churchwell 1997; Claussen et al. 1997; Thompson & Macdonald 1999; Kim & Koo 2001, 2003; Sollins et al. 2004; Hunter et al. 2008; Nicholas et al. 2011).

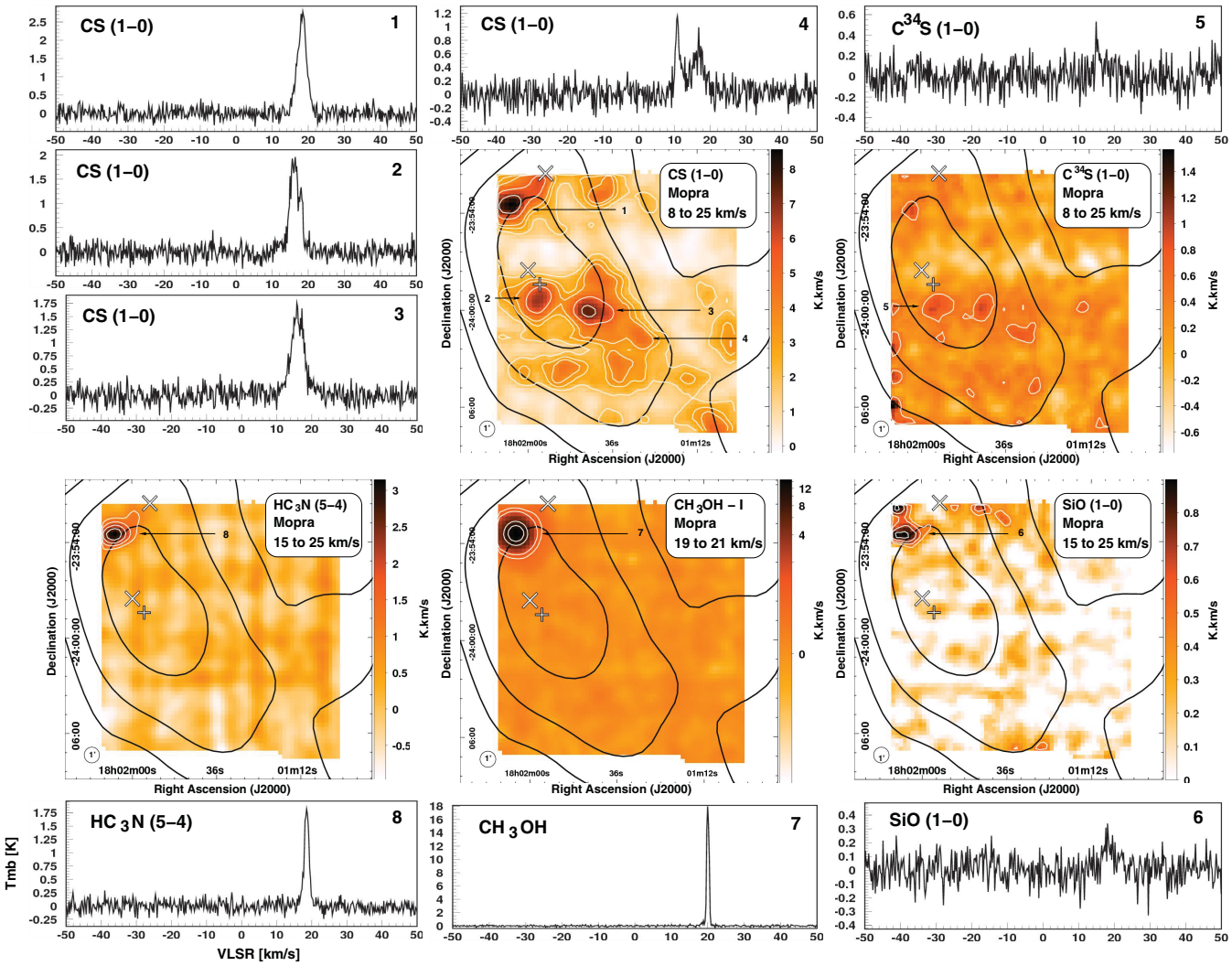

Figure 5. Integrated intensity images and spectra for the emission seen towards HESS J1800−240 A. Integration ranges are indicated on each panel. In all panels, black contours are the HESS TeV emission (4–6σ), black/white crosses ($\times$) indicate the positions of the H II regions G6.225−0.569 (north) and G6.1−0.6 (south), the cross + is the location of IRAS 17588−2358, and the white contours are used to highlight the molecular emission from the image. Minimum white contour level for CS (1–0) is 1.75 K km s^{-1} ($\sim$5 $T_{\rm RMS}$); for $C^{34}S$ is 0.52 K km s^{-1} ($\sim$2 $T_{\rm RMS}$); for HC_3N (5–4) is 1.04 K km s^{-1} ($\sim$4 $T_{\rm RMS}$); for CH_3OH is 0.22 K km s^{-1} ($\sim$3 $T_{\rm RMS}$) and for SiO (1–0) is 0.42 K km s^{-1} ($\sim$3 $T_{\rm RMS}$). Surrounding the integrated images are spectra taken from the mapping data and are labelled according to their locations.

Outflow velocities $\pm$70 km s^{-1} are seen in CO lines and similar claims are made for SiO lines by Acord et al. (1997). Sollins et al. (2004) argue that the outflow originates from a 1.3 mm continuum source and not from Feldt's candidate star (Feldt et al. 2003), as the star is not equidistant from the outflow lobes. The H II complex G5.89−0.39 actually comprises two active star formation regions, H II G5.89−0.39 A to the east and UCH II G5.89−0.39 B approximately 2 arcmin to the west (Kim & Koo 2001). G5.89−0.39 A is also known as W28 A2 with strong radio continuum emission, while G5.89−0.39 B possesses the outflow. We observe SiO (1–0) over a wide region towards the three sources suggesting there are shocks or outflows. Multiple higher order SiO transitions on smaller scales are detected towards the G5.89−0.39 B region and have been discussed by Acord et al. (1997).

A new perspective that this work provides is the broad scale (15 arcmin) dense gas surrounding the H II regions. NW of the UC H II region G5.89−0.39 B in CS (1–0) we see an extended arm feature with length $\sim$6 arcmin extending north towards W28 (e.g. points 3 and 4 in Fig. 6). The dense gas seen in this arm appears to have a slight velocity gradient, approximately +0.3 km s^{-1} arcmin^{-1} from north to south. To the SE of the H II regions there are several dense clumps which trace the dense component of the cloud seen in CO (2–1) by Fukui et al. (2008). Once again, these cores display broad CS (1–0) emission (FWHM $>$ 4 km s^{-1}), however, these clumps are at a slightly larger $V_{\rm LSR}$ compared to the H II regions. Interestingly, most of the CS (1–0) emission from the southern cloud contains multiple clumps along the line of sight, all within $\sim$20 km s^{-1} of each other. This makes $v_{\rm RMS}$ calculations difficult as the multiply clumped emission produces artificially broad results.

Star formation tracers such as 44 GHz Class I CH_3OH masers and HC_3N (5–4) emission have been detected towards all three of the aligned sources. We also detect signs of warm gas phase chemistry via detections of HC_3N (5–4) towards dense cores SE of the H II regions (e.g. point 22 in Fig. 6) which lie in a dense molecular ridge (see Fig. 1). We also detect the HC_5N (16–15) and (17–16) lines

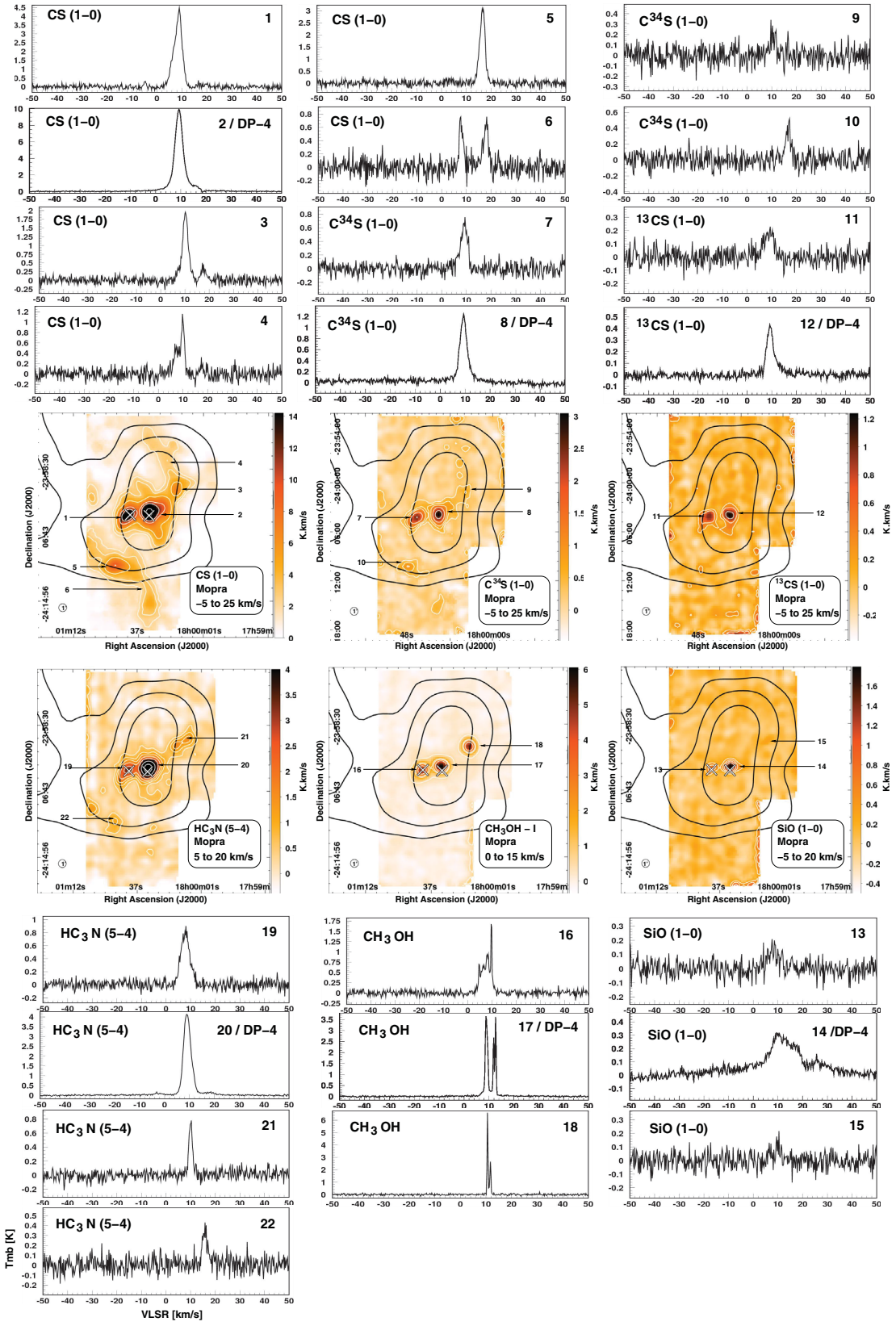

Figure 6. Integrated intensity maps and spectra for the southern HESS J1800−240 B region. In all panels, black/white crosses (×) indicate the positions of G5.89−0.39 A (left) and B (right) and thick black contours are the HESS TeV emission (4–6σ). White contours are used to highlight the molecular emission from the image. Minimum contour level for: CS (1–0) is 2.08 K km s^{-1} (∼8 $T_{\rm RMS}$); C^{34}S (1–0) is 0.32 K km s^{-1} (∼2 $T_{\rm RMS}$); ^{13}CS (1–0) is 0.24 K km s^{-1} (∼2 $T_{\rm RMS}$); HC_3N (5–4) is 0.57 K km s^{-1} (∼3 $T_{\rm RMS}$); CH_3OH-I is 0.5 K km s^{-1} (∼5 $T_{\rm RMS}$) and SiO (1–0) is 0.36 K km s^{-1} (∼3 $T_{\rm RMS}$). Surrounding the integrated images are spectra taken from both the mapping data and deep pointings, labelled according to their locations.

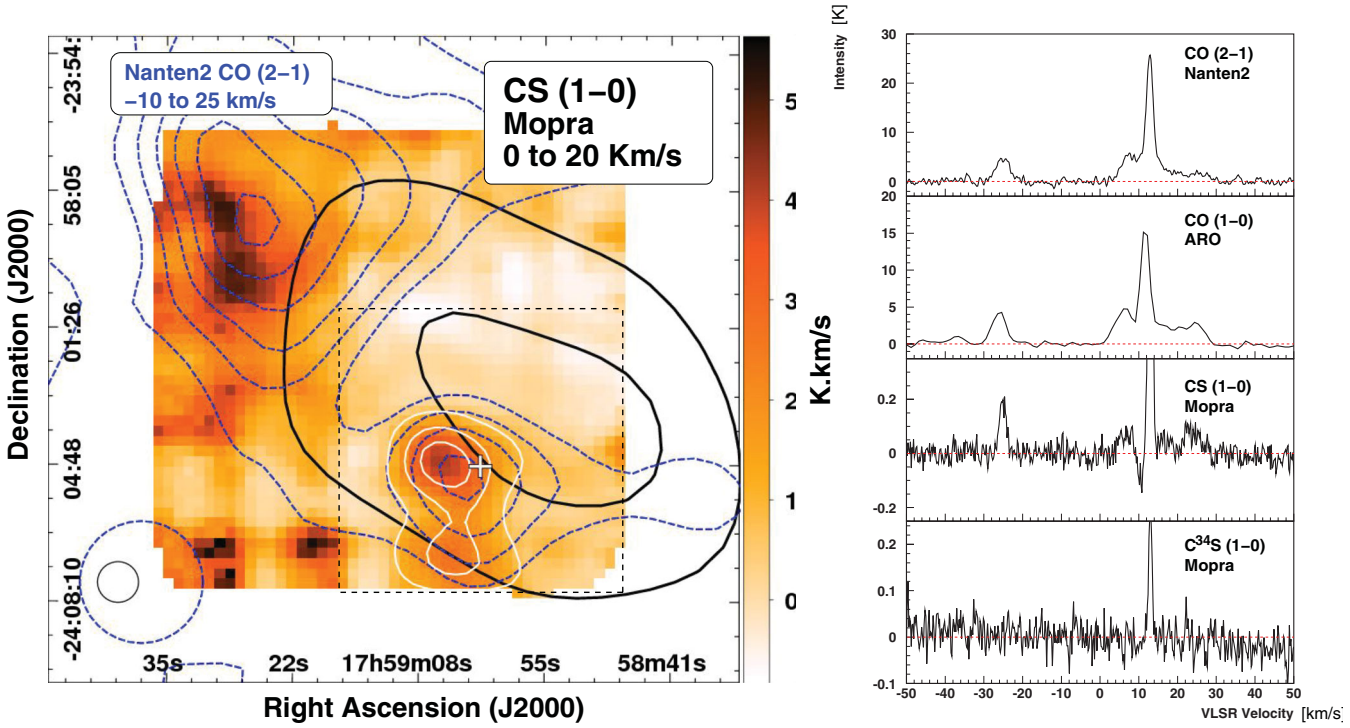

Figure 7. Left: integrated intensity image of CS (1–0) emission towards HESS J1800−240 C, which contains the recently detected 1720 MHz OH maser (G5.7−0.0) by Hewitt & Yusef-Zadeh (2009). The maser position is indicated by the cross +. Blue dashed contours are Nanten CO (2–1) integrated intensity contours from Fukui et al. (2008). White contours are used to highlight CS (1–0) emission, only for the region of highest exposure (indicated by the black dashed box. Minimum white contour level is 0.88 K km s^{-1} ($\sim 2\,T_{\rm RMS}$). Right: spectra for the CO (2–1) (Fukui et al. 2008) CO (1–0) (Liszt 2009), CS (1–0) and C^{34}S (1–0) for the maser position. Spectra for the CS isotopologue emission are taken from the Mopra deep pointing at the location of the OH maser. For the CS (1–0) emission, the vertical scale has been clipped (peak temperature 2.5 K) to show the evidence for line-wings and absorption in the profile.

towards G5.89−0.39 B. This would indicate that there is considerable energy available to excite the molecules into such a highly excited state.

An additional site of stellar activity is seen towards our southernmost mapped region. At the base of the dense ridge seen in CS (1–0), we detect SiO emission in the $v = 1, 2, 3$ modes of the (1–0) line. Here we are probably tracing the radiationally excited SiO emission from the variable star V5357 Sgr. Spectra for the SiO emission are displayed in Fig. A2 (in the online version of the journal – see Supporting Information).

We have also taken position switched deep pointings towards G5.89−0.39 B (DP-4) and towards the northern most point of the arm NE of G5.89−0.39 (DP-3). We have estimates of the mass and density from the CS isotopologue emission towards G5.89−0.39 B. We do not detect any isotopologue emission from the extended arm position (DP-3) so we estimate the gas parameters under the assumption that the CS (1–0) emission is optically thin. The results of the compact-source analysis are displayed in Table 2.

4.4 HESS J1800−240 C/G5.71−0.08

The CS (1–0) emission detected towards HESS J1800−240 C shows two emitting regions along the line of sight, one with $V_{\rm LSR} \sim -25$ km s^{-1} and another with $V_{\rm LSR} \sim 13$ km s^{-1}. This dense CS core is slightly offset from the peak of the TeV source and may provide a suitably dense region for CR interactions. The CS emission is also spatially matched with the SNR candidate G5.71−0.08 and the 1720 MHz OH maser at $V_{\rm LSR} = 13$ km s^{-1} (Hewitt & Yusef-Zadeh 2009). The OH maser may indicate that HESS J1800−240 C is tracing another SNR/MC interaction. Fig. 7 shows an integrated intensity image of the HESS J1800−240 C region comparing our CS (1–0) emission and the CO (2–1) emission from Fukui et al. (2008). Spectra from our C^{34}S (1–0) and CS (1–0) deep pointings, the CO (2–1) spectra from Fukui et al. (2008) and CO (1–0) spectra from Liszt (2009) at the position of the 1720 MHz OH maser are also presented.

The spectra presented in Fig. 7 reveal line-wings in the CO (2–1) and (1–0) profiles, with $V_{\rm LSR} \sim 0$–8 and 20–30 km s^{-1}, indicative of turbulent conditions. The CS (1–0) profile also shows some structure in these $V_{\rm LSR}$ ranges, which could be interpreted as multiple clumps along the line of sight, or evidence for line-wings. There is also an absorption dip at $V_{\rm LSR} \sim 10$ km s^{-1}. Similarly, absorption features are present in the 1720 MHz OH spectrum at $V_{\rm LSR} = 7$ and -25 km s^{-1} (Hewitt & Yusef-Zadeh 2009), and may also be evident in the CO emission. This is likely due to absorption against a continuum source. Interestingly, the width of the CS (1–0) line profile is narrow, with FWHM = 1 km s^{-1}. This could suggest the central region of the core is rather quiescent.

The two isotopologues of CS are detected in our deep position switched observation towards the new OH maser position and allow the mass and density to be estimated. For this CS core we estimate a mass of 190 $M_\odot$ and an H_2 number density of 1.7×10^5 cm^{-3}. Finally, we note that this mapped region associated with HESS J1800−240 C has less exposure (a factor of 1.5 to 3 lower) than the HESS J1801−233 and HESS J1800−240 B regions.

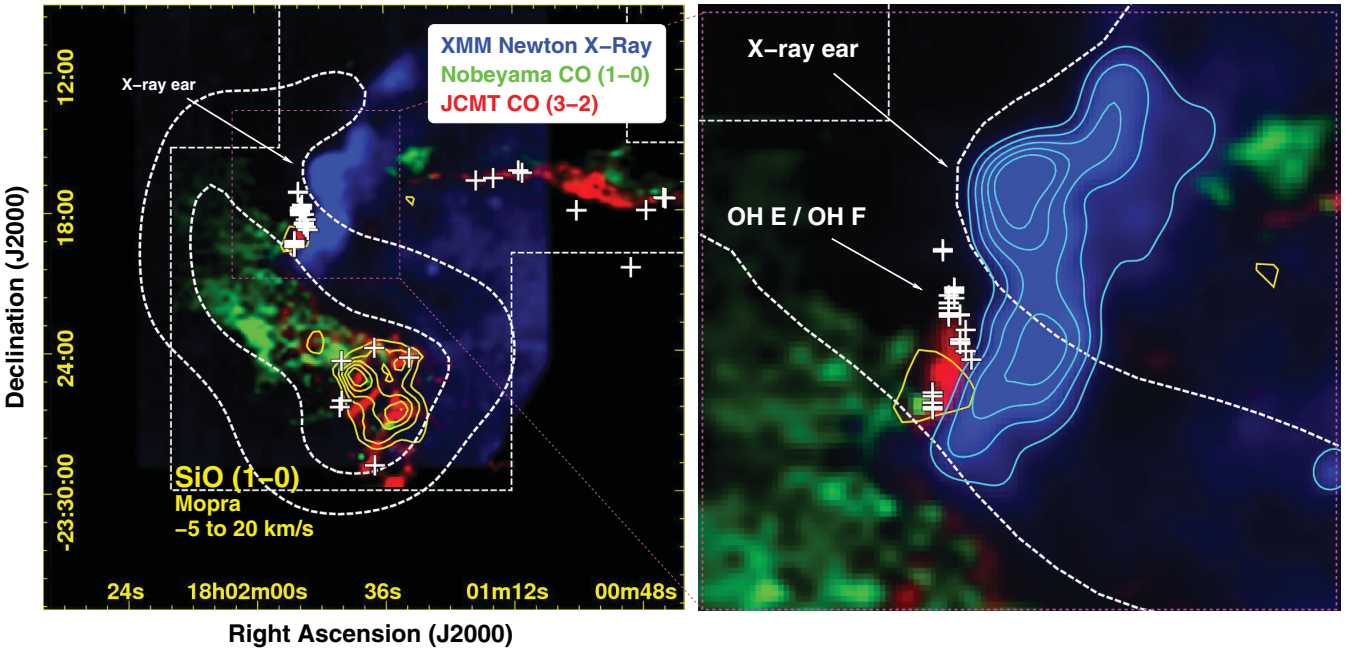

Figure 8. Left: three colour image for the HESS J1801−233 region. The red channel is James Clerk Maxwell Telescope CO (3–2) integrated from −40 to 40 km s^{-1} (Arikawa et al. 1999). The green channel is the Nobeyama CO (1–0) emission integrated from 4 to 9 km s^{-1} (Arikawa et al. 1999). The blue channel is the *XMM–Newton* 0.2 to 10 keV [photons cm^{-2} s^{-1}] image (Gaussian smoothed). White dashed lines indicate the limits of the CO images. Thick white dashed contours are HESS TeV emission (4 and 5σ levels). Yellow solid contours are Mopra SiO (1–0) integrated from −5 to 20 km s^{-1}, as seen in Fig. 3. White crosses + indicate the positions of 1720 MHz OH masers from Claussen et al. (1997). Right: zoom of the X-ray ear and OH maser clusters OH E and OH F from Claussen et al. (1997).

5 X-RAY AND TEV GAMMA-RAY EMISSION AND DISCUSSION

5.1 HESS J1801−233/NE shocked cloud

The CS (1–0) emission seen towards the NE cloud traces an extended dense region of molecular material. Using the emission within a region defined by $\int T_{mb} dv \geq 10\,K\,km\,s^{-1}$ ($\sim 40\,T_{RMS}$) and finding the average CS (1–0), $C^{34}S$ (1–0) and ^{13}CS (1–0) emission profiles within the region, we can estimate the gas parameters as an extended source. We apply this strict limit on the CS (1–0) emission to only accept pixels containing CS, $C^{34}S$ and ^{13}CS emission, and not bias the optical depth result. Under these conditions, we estimate the CS emission fills an ellipse on the sky with physical dimensions of 3.1 × 1.4 pc (at the estimated 2 kpc distance). This elliptical region is indicated in Fig. 2. Additionally, we assume the volume of the emission is defined by a prolate ellipsoid, where the third axis (in the z direction) is the same as the minor axis of the ellipse on the sky. In this way, the ellipsoid has radii 3.1 × 1.4 × 1.4 pc. Using the method outlined in Section 3, we calculate the mass using Nicholas et al. (2011, equation 3) and include an additional factor $\eta_{mb}/\eta_{xb} = 0.77$ to account for the Mopra extended beam efficiency $\eta_{xb} = 0.43$ (Urquhart et al. 2010). This gives an estimated extended source mass of $5.6 \times 10^4\,M_\odot$ and an H_2 number density of $6.1 \times 10^4\,cm^{-3}$. The extended source mass and density estimates are presented in Table 3.

We compare our CS gas mass to other mass estimates of the region. Over the 0–12 km s^{-1} velocity range, the CO (1–0) mass has been estimated to be $\sim 2 \times 10^4\,M_\odot$, and over the wider 0–25 km s^{-1} velocity range $\sim 5 \times 10^4\,M_\odot$ (Aharonian et al. 2008a). From CO (3–2) data Arikawa et al. (1999) estimated there to be $2 \times 10^3\,M_\odot$ of shocked gas in the NE cloud and $4 \times 10^3\,M_\odot$ of unshocked gas. Additionally a conservative lower limit to the mass of gas traced by NH_3 inversion transitions has been estimated to be $>1300\,M_\odot$ (Nicholas et al. 2011).

At a glance the mass derived from CS is larger than previously published estimates. It is at least 10 times the lower limit obtained via NH_3 observations. This is likely due to the considerable uncertainties in molecular abundance ratios, which are usually the largest sources of systematic error in mass/density calculations. While an order of magnitude mass discrepancy is not ideal, it has been shown for a sample of molecular cores, both hot and cold, that the core masses have equal or higher values from CS observations than those found via NH_3, in some cases discrepancies up to two orders of magnitude (Zhou et al. 1989). We suggest the CS mass be an upper limit as the abundance in a shocked source is likely to be lower than that we have assumed applies in an undisturbed, dense MC. The fact that the morphological extent of the CS emission is similar to that in CO, however, suggests that a quite high fraction of the molecular gas is in a high-density state.

The X-ray morphology of W28 is described as centre filled (Rho & Borkowski 2002) whereby X-ray emission lies towards the centre of the SNR. Interestingly, there is a brightening of the X-ray emission towards the NE of the SNR. This so-called '*ear*' feature, labelled by Rho & Borkowski (2002), is found at the boundary of the pre- and post-shocked MC seen in CO (1–0) and (3–2) (Arikawa et al. 1999).

XMM–Newton X-ray observations towards the NE shocked cloud have been discussed in Ueno, Bamba & Koyama (2003) following earlier observations with *ASCA* and *ROSAT* (Rho & Borkowski 2002). Here, we have looked at additional *XMM–Newton* archival observations totalling ∼56 ks of observation time. Data were reprocessed using the *XMM* SAS software suite (with standard quality cuts) and major proton flares were filtered out. Observation IDs used

were 0135742401 (5.5 ks post filter), 0145970101 (20 ks – analysed by Ueno et al. 2003) and 0145970401 (30 ks).

The X-rays result mostly from thermally heated gas (post shocked) with $kT = 0.3$ keV (Ueno et al. 2003). Fig. 8 presents the *XMM–Newton* full EPIC camera (PN+MOS1+MOS2) image in the 0.2 to 10 keV band corrected for exposure in the blue channel. The red and green channels are the post-shocked CO (3–2) and pre-shocked CO (1–0) gas from Arikawa et al. (1999). The right-hand panel of Fig. 8 is a zoom of the X-ray '*ear*' feature, revealing the boundary between the X-ray emission and the shocked gas. Also seen at this boundary are many 1720 MHz OH masers (Claussen et al. 1997, groups OH E and OH F, labelled in Fig. 4). Interestingly, adjacent to the OH maser groups E and F we also detected SiO (1–0) at the $2\,T_{\rm RMS}$ level, further enhancing the evidence that there is shocked and disrupted dense gas in the region.

The cluster of masers (OH E and OH F) are possibly associated with the X-ray *'ear'* (Fig. 8). What is particularly intriguing is that the OH E and F clusters of 1720 MHz OH masers appear to lie on both sides of the shocked gas (Fig. 8, red channel) with respect to W28. This may result from projection effects which are hard to disentangle or the possibility of an additional or reverse shock propagating inwards towards W28. The OH E and F maser clusters lie in the 10–15 km s^{-1} velocity range (Fig. 4). This suggests that the post-shocked X-ray emitting gas may lie behind most of the NE dense MC, which peaks in the 5–10 km s^{-1} velocity range (Fig. 4).

The broad molecular line emission observed towards the NE cloud would likely result from non-thermal components. The additional kinetic energy required to produce the broad line emission can be calculated. We determine the non-thermal energy as $W_{\rm kin} = 1/2M(\Delta v_{\rm kin})^2$, where M is the mass of the broad line gas, and $\Delta v_{\rm kin}$ is the line FWHM. Using the average CS (1–0) line FWHM $= 7.3$ km s^{-1} and the average extended mass upper limit $M = 5.6 \times 10^4$ M$_\odot$, we obtain $W_{\rm kin} < 3.8 \times 10^{49}$ erg, which is a few per cent of the total 10^{51} erg released in a typical SNR explosion. This upper limit is in agreement with our earlier estimate of the kinetic energy deposited into the dense NE cloud ($W_{\rm kin} > 7 \times 10^{47}$ erg) from our earlier NH_3 observations. Similarly, Arikawa et al. (1999) estimated $\sim 3 \times 10^{48}$ erg of kinetic energy has been deposited into the 2000 M$_\odot$ traced by shocked CO (3–2).

The impact of CRs and SNR shocks on MCs has been discussed extensively. Aharonian, Drury & Völk (1994) discuss a MC being overtaken by an SNR shock. The 'crushed cloud' model from Uchiyama et al. (2010) discusses the re-acceleration of particles within a MC, but is mainly applicable to GeV energies. Yamazaki et al. (2006) discuss three cases for VHE emission from old or evolving SNRs and MCs. This includes (i) emission from the SNR shock alone, (ii) the SNR shock colliding with an MC and (iii) CRs accelerated a distance away from a MC and diffusing through the interstellar medium (ISM) to illuminate the cloud. This latter case of CR acceleration and diffusion is also more recently discussed in Abdo et al. (2010), Gabici et al. (2010), Ohira, Murase & Yamazaki (2011), with discussion specifically towards W28. Fujita et al. (2009) discuss the scenario of CRs accelerated by an SNR shock nearby or just outside the W28 MCs. Recent work by Inoue, Yamazaki & Inutsuka (2010) models the propagation of middle-aged SNR shocks into a cloudy ISM, revealing the presence of multiple secondary shocks with total surface area comparable to the primary shock. These shocks are able to accelerate particles to a maximum energy $E_{\rm max} > 10$ TeV (Inoue et al. 2010). Overall, all models can account for the TeV and GeV emission seen towards W28 and other similarly aged SNRs. They clearly favour the hadronic emission mechanism for TeV emission.

Under a hadronic emission mechanism, TeV photons result from CR collisions producing π^0 mesons. The π^0s then decay into the TeV photons. The leptonic emission mechanism produces TeV photons by inverse Compton processes and/or electron non-thermal bremsstrahlung. However, these leptonic processes are suppressed in evolved SNRs due to electron cooling via synchrotron losses at much earlier epochs.

TeV gamma-rays are observed with energies in the 0.3–3 TeV range (Aharonian et al. 2008a). In the hadronic scenario, typically 17 per cent of the CR particle's energy is transferred to gamma-rays, therefore 0.3–3 TeV gamma-rays trace a parent population of ∼2–20 TeV CRs at the source. The striking spatial overlap between the TeV emission and the dense gas towards HESS 1801−233 suggests that CRs are reaching the dense portions of the MC, and could help provide constraints for CR diffusion models (Gabici, Aharonian & Blasi 2007). However present HESS observations do not have sufficient angular resolution (∼10 arcmin FWHM) to test whether the CR spectrum varies towards the interior of the dense cores. Future TeV instruments with sufficient angular resolution (arcmin) are required before such spectral features may become apparent and help to discriminate between models of re-acceleration and diffusion. A future TeV instrument, such as the Cherenkov Telescope Array (CTA) (The CTA Consortium 2010), will have both improved angular resolution and sensitivity. The expected angular resolution could reach a few arcmin FWHM and the energy sensitivity is expected to be a factor of 10 better than HESS, achieving ∼ a few $\times 10^{-14}$ erg cm^{-2} s^{-1} in ∼50 h. Together, these improvements will permit TeV emission maps and detailed spectra with comparable spatial scales to the molecular gas maps and provide a platform to test CR diffusion models and probe re-acceleration models.

The expected flux of TeV emission from an MC impacted by Galactic CRs (GCR) with particle flux following an integral power law $E^{-1.6}$ can be found from Aharonian (1991, equation 10):

$$F(\geq E_\gamma) = 2.85 \times 10^{-13}\, E_{\rm TeV}^{-1.6} \left(\frac{M_5}{d_{\rm kpc}^2}\right) k_{\rm CR} \quad (\text{photons cm}^{-2}\,\text{s}^{-1}), \tag{1}$$

where M_5 is the mass of the cloud (in 10^5 M$_\odot$), $d_{\rm kpc}$ is the distance to the cloud (kpc) and $k_{\rm CR}$ is the CR density enhancement factor above the local Solar system value. The observed TeV spectral indices (Aharonian et al. 2008a) imply an incident proton particle spectral integral index of $\Gamma \sim 1.6$ (in a power-law particle spectrum $\propto E^{-\Gamma}$) similar to GCRs. Thus equation (1) should be sufficient for initial estimates of the TeV fluxes arising from parts of the clouds. We note that further discussion of other systematic uncertainties concerning the predicted TeV fluxes from cloud clumps is left for Section 6.

The CR enhancement factors have been estimated towards three of the four TeV sources in (Aharonian et al. 2008a, table 2). With this in mind, we can estimate the gamma-ray flux for emission from the dense cloud components traced by CS (1–0) emission. Using the NE shocked cloud extended source mass estimate from Table 3, we estimate $F(\geq 1\,\text{TeV}) = 5.1 \times 10^{-13}$ photons cm^{-2} s^{-1}. The flux results for this, and other CS regions, are summarized in Table 4. We note that this flux is ∼15 per cent higher than that currently detected by HESS This further supports our case for treating the CS mass estimate as an upper limit given the uncertainties in the CS abundance. The general picture though is that the predicted TeV flux is detectable and can be well studied by CTA in a reasonable observation time (10–50 h). CTA could then discriminate between the TeV emission from within the dense cloud component versus that of the entire cloud as seen by HESS.

5.2 HESS 1800−240 A and B

The southern TeV sources HESS J1800−204 A and B are also associated with dense gas which could provide a suitable target for CR interactions. The dense regions of gas spatially consistent with HESS 1800−240 A are treated as elliptical extended sources filling prolate ellipsoids with radii 1.4 × 0.7 × 0.7 pc for the gas nearby G6.225−0569 and 2.8 × 1.4 × 1.4 pc for the gas nearby G6.1−0.6. Similarly, the CS gas seen towards HESS J1800−240 B is treated as three separate extended sources. The large clump associated with the G5.89−0.39 H II regions is assumed to fill a prolate ellipsoid with radii 2.4 × 2.1 × 2.1 pc. The CS emission from the NW arm, extending from V5561 Sgr, is assumed to fill an ellipsoid with radii 3.1 × 1.1 × 1.1 pc, and the SE molecular ridge is assumed to fill an ellipsoid with radii 3.5 × 1.4 × 1.4 pc. These elliptical regions are indicated in Fig. 2. We detect only CS (1–0) emission from the NW arm and SE ridge regions, therefore, we assume the emission to be optically thin. The individual estimates for the mass and density of all the extended regions towards HESS J1800−240 A and B are summarized in Table 3.

The three extended regions towards HESS J1800−240 B suggest that $7.1 \times 10^4\,M_\odot$ of material is contained in dense clumps. The HESS J1800−240 B southern cloud is estimated to have $10^5\,M_\odot$ based on the CO (1–0) emission (Aharonian et al. 2008a). Based on our extended CS clump estimates, we find that ∼70 per cent of the southern clouds mass is contained in the dense clumps surrounding the G5.89−0.39 H II regions.

As these three dense extended regions all lie within the HESS J1800−240 B source, the improved angular resolution of CTA could potentially resolve this emission into three separate sources. In this case, the expected gamma-ray flux can be found via equation (1). The expected TeV flux for photon energy $E > 1$ TeV for each of the dense cloud components is summarized in Table 4. Typically the expected flux is 10^{-13} to 10^{-14} photons cm^{-2} s^{-1}, which could be detectable and well studied by CTA in a reasonable observation time (10–50 h). As for the NE cloud, we find that the total expected flux from the three HESS J1800−240 B sources is higher than the detected level of TeV emission (by a factor of ∼2). Again, this could be explained by our choice of CS abundance being overestimated in this region which may be expected given likely internally shocked nature of the G5.89−0.39 H II complex. Additionally, our cloud-averaged CR density k_{CR} may not reflect smaller scale variations.

The question of the origin of the CR population towards HESS J1800−240 A and B is still uncertain, although diffusion of CRs from W28 seems to reasonably well explain the observed GeV to TeV gamma-ray spectra (e.g. Fujita et al. 2009; Abdo et al. 2010; Gabici et al. 2010; Li & Chen 2010). However, additional CRs accelerated inside the local star formation regions (from G5.89−0.39 in particular), and another potential SNR towards HESS J1800−240 C (discussed shortly), remains a possibility (see e.g. Araudo et al. 2007). Our observation of the arcmin-scale dense NW arm and SE ridge features in the MC may signal additional sites of disruption which could arise from internal (star formation) and/or external (e.g. SNR shocks) forces. Further tests of these scenarios can come from future arcmin-scale studies of gamma-ray spectra throughout the clouds.

Table 4. Summary of the CR enhancement factors, k_{CR}, and the predicted TeV fluxes from the extended dense regions listed in Table 3. The predicted fluxes assume a CR enhancement factor determined in Aharonian et al. (2008a), except for HESS J1800−240 C, k_{CR} has been calculated here. We treat the flux from the NE shocked cloud as an upper limit, as the estimated mass is an upper limit.

Region	k_{CR}	Expected flux $F(E \geq 1\,\mathrm{TeV})$ (photons cm^{-2} s^{-1})
NE shocked cloud	13	$< 5.1 \times 10^{-13}$
G5.89−0.39 H II region	18	7.0×10^{-13}
G5.89−0.39 NW arm	18	5.4×10^{-14}
G5.89−0.39 SE ridge	18	1.6×10^{-13}
G6.1−0.6 region	14[a]	6.5×10^{-14}
G6.225−0.569 region	14[a]	1.6×10^{-14}
HESS J1800−240 C	35[b]	4.7×10^{-15}

[a] k_{CR} from Aharonian et al. (2008a) has been re-scaled assuming a $d = 2$ kpc.
[b] k_{CR} calculated using the CO (1–0) emission from Mizuno & Fukui (2004) and assuming the compact-source mass (DP-5) indicated in Table 2.

5.3 HESS J1800−240 C

Towards HESS J1800−240 C, we have discovered a dense molecular core. Unlike the other TeV sources in the W28 region, the dense gas lies slightly offset from the peak of the TeV emission. The CS gas is found in a dense, compact core, which has a narrow linewidth, FWHM 1 km s^{-1}. Additionally, there is absorption in the CS line profile at ∼10 km s^{-1}, which may also be evident in the CO (1–0) and (2–1) line profiles (see spectra in Fig. 7).

Based on the CO (1–0) emission from the Nanten survey (Mizuno & Fukui 2004), we estimated the mass of the CO cloud. We assumed a CO abundance of $\chi_{CO} = 1.5 \times 10^{20}$ and assumed a spherical emission region with radius 0.°1 centred on the HESS J1800−204 C TeV source. We included emission from the 0–20 km s^{-1} range, which was selected to be consistent with the ranges used in Aharonian et al. (2008a). Under these assumptions, we estimated $1.4 \times 10^4\,M_\odot$ of CO gas towards HESS J1800−240 C. We estimated the CR enhancement factor $k_{CR} = 35$, using equation (1), based on the CO mass and the detected TeV flux following Aharonian et al. (2008a). Assuming the value of $k_{CR} = 35$ we determined the expected TeV flux from just the dense CS core. The result is shown in Table 4.

The determined CR enhancement of 35 is higher than towards the other TeV sources. Enhancements of this level are expected in the regions of CR accelerators, which could be expected as this region could be associated with both the W28 SNR and the local SNR candidate G5.71−0.08 which may be producing the OH maser. Under a purely hadronic emission scenario, the expected TeV flux from just the dense CS core is $F(E \geq 1\,\mathrm{TeV}) \sim 5 \times 10^{-15}$ photons cm^{-2} s^{-1}. This flux level would likely push the reasonable detection limits for CTA.

6 SUMMARY AND CONCLUSIONS

Using the Mopra 22-m telescope, we have conducted 7 mm molecular line mapping covering dense and disrupted gas towards the W28 SNR field. We have followed up our previous 12 mm line study of the MCs towards the TeV gamma-ray peaks observed by the HESS telescope, with higher resolution targeted observations towards the NE cloud/shock interaction, HESS J1801−233 and the bright and energetic UC-H II regions in the southern cloud HESS J1800−240 B.

Sites of shocks, outflows and disruption are revealed with SiO. In the majority of cases, SiO detections are towards sites of stellar activity and H II regions; however, SiO is also detected in the

NE cloud/SNR shock interaction region with broad line profiles. Interestingly, in this shock region the SiO emission is bounded by clusters of 1720 OH masers, indicating the downstream direction of the shock is towards W28. Other lines detected are 44 GHz CH_3 OH masers and cyanopolyynes HC_nN ($n = 3, 5, 7$) which are again preferentially associated with star formation and H II regions.

The CS cores are typically found towards CO peaks and trace conditions ranging from quiescent cloud cores to H II regions. The obvious exception is the NE cloud/SNR shock interaction region, which exhibits broad line emission FWHM $> 10\,\mathrm{km\,s^{-1}}$ in all detected lines.

Based on CS isotopologue ratios from our position-switched deep pointing observations, we are able to estimate the upper state CS column density. Temperature estimates from our previous NH_3 observations allow the LTE molecular hydrogen mass and density to be estimated. Our results presented in Table 2 assume a compact-source core radius $r = 0.2$ pc; however, scaling factors for various core radii are also included.

We have estimated the mass of the extended dense NE cloud and several of the dense clumps in the southern clouds, assuming the CS isotopologue emission is contained within a prolate ellipsoid. Under these assumptions, we estimate there to be $5.6\times\ 10^4\,\mathrm{M_\odot}$, with H_2 number density $6.1\times 10^4\,\mathrm{cm^{-3}}$ (as an upper limit) contained towards the NE HESS J1801−233 TeV source. We find that $\sim 4\times 10^{49}$ erg of kinetic energy is required to produce the broad emission in the CS line profile towards the NE cloud, which is a few per cent of the typical 10^{51} erg of kinetic energy released in an SNR.

For the southern cloud towards HESS J1800−240 B we estimate that ∼70 per cent of the gas mass is contained in dense clumps surrounding the H II regions. The southern clouds show no signs of external disruption, providing no evidence that the W28 SNR shock has influenced the region.

Although our CS masses are treated as upper limits, we note that a somewhat independent estimate of the CS mass for clumps not part of the NE Shocked Cloud comes from the virial theorem. For these cases the fact that the virial mass is similar to the LTE mass within a factor 2 to 3 suggests our choice of CS abundance is adequate for order of magnitude estimates. For the NE Shocked Cloud the virial theorem will likely not apply. However, as discussed in Section 5.1, the NE Shocked Cloud mass derived from our CS observations is 10 per cent larger than the mass from CO observations, indicating that our CS abundance may be slightly overestimated here.

Additional systematic uncertainties arise from the unknown spectrum of CRs entering the dense clouds, and, penetrating their interiors as a result of energy-dependent diffusion. Equation (1) assumes that a CR spectral integral index of $\Gamma = -1.6$ as expected for GCRs impacting passive clouds some distance away. The spectral indices of the TeV emission towards W28 are in fact found to be similar to GCRs so equation (1) should be adequate in this regard.

The striking spatial match between the TeV emission and the dense molecular gas suggests that the CRs are able to penetrate some distance into the dense cloud core. However, the energy-dependent diffusion of CRs into the cloud cores (Gabici et al. 2007) could easily suppress the predicted emission for low energies $E < 1$ TeV below that suggested by equation (1). The level of suppression is strongly dependent on the largely unknown magnetic field structure and turbulence in the clump and is a topic beyond the scope of this paper.

Overall, we would like to emphasize that the uncertainties discussed above clearly motivate the need for new 1 arcmin angular resolution TeV observations (e.g. by CTA) in order to begin probing the diffusion properties of CR into dense MCs.

This work is part of our ongoing study into the molecular gas towards the W28 region, and follows our earlier 12 mm line mapping campaign. Additional observations of the NE cloud SNR interaction region have been conducted with Mopra at 12 mm in order to extract detailed NH_3 inversion spectra across the cloud core. Results of these observations will be the focus of a future paper to further understand the molecular gas properties in the interesting NE SNR shock/MC interaction region.

ACKNOWLEDGMENTS

We thank Cormac Purcell for his baseline fitting and removal script. This work was supported by Australian Research Council grants (DP0662810, DP1096533). The Mopra telescope is part of the Australia Telescope and is funded by the Commonwealth of Australia for operation as a National Facility managed by CSIRO. The University of New South Wales Mopra Spectrometer Digital Filter Bank used for these Mopra observations was provided with support from the Australian Research Council, together with the University of New South Wales, University of Sydney, Monash University and the CSIRO.

REFERENCES

Abdo A. A. et al. (Fermi Collaboration), 2010, ApJ, 718, 348
Acciari V. A. et al. (VERITAS Collaboration), 2009, ApJ, 698, L133
Acord J. M., Walmsley C. M., Churchwell E., 1997, ApJ, 475, 693
Aharonian F. A., 1991, Ap&SS, 180, 305
Aharonian F. A., Drury L. O'C., Völk H. J., 1994, A&A, 285, 645
Aharonian F. et al. (HESS Collaboration), 2004, A&A, 425, L13
Aharonian F. et al. (HESS Collaboration), 2006, Nat, 439, 695
Aharonian F. et al. (HESS Collaboration), 2008a, A&A, 481, 401
Aharonian F. et al. (HESS Collaboration), 2008b, A&A, 490, 685
Albert J. et al. (MAGIC Collaboration), 2008, ApJ, 674, 1037
Araudo A. T., Romero G. E., Bosch-Ramon V., Paredes J. M., 2007, A&A, 476, 1289
Arikawa Y., Tatematsu K., Sekimoto Y., Takahashi T., 1999, PASJ, 51, L7
Brogan C. L., Gelfand J. D., Gaensler B. M., Kassim N. E., Lazio T. J. W., 2006, ApJ, 639, L25
Bronfman L., Nyman L.-Å., May J., 1996, A&AS, 115, 81
Choi M., Evans N. J., II, Jaffe D. T., 1993, ApJ, 417, 624
Churchwell E., Walmsley C. M., Cesaroni R., 1990, A&AS, 83, 199
Claussen M. J., Frail D. A., Goss W. M., Gaume R. A., 1997, ApJ, 489, 143
Codella C., Palumbo G. G. C., Pareschi G., Scappini F., Caselli P., Attol ini M. R., 1995, MNRAS, 276, 57
Crutcher R. M., 1991, ApJ, 520, 706
Dubner G. M., Velázquez P. F., Goss W. M., Holdaway M. A., 2000, AJ, 120, 1933
Feinstein F., Fiasson A., Gallant Y., Chaves R. C. G., Marandon V., de Naurois M., Kosack K., Rowell G. (for HESS Collaboration), 2009, in Bastieri D., Rando R., eds, AIP Conf. Proc. 1112, Science with the New Generation of Gamma-Ray Experiments. Am. Inst. Phys., New York, p. 54
Feldt M. et al., 2003, ApJ, 599, L91
Fontani F., Cesaroni R., Furuya R. S., 2010, A&A, 517, A56
Frail D. A., Goss W. M., Slysh V. I., 1994, ApJ, 424, L111
Frerking M. A., Wilson R. W., Linke R. A., 1980, ApJ, 240, 65
Fujita Y., Ohira Y., Tanaka S. J., Takahara F., 2009, ApJ, 707, L179
Fukui Y. et al. (NANTEN Collaboration), 2008, in Aharonian F. A., Hofmann W., Rieger F., eds, AIP Conf. Proc. 1085, High Energy Gamma-Ray Astronomy. Am. Inst. Phys., New York, p. 104
Gabici S., Aharonian F. A., Blasi P., 2007, Astrophys. Space Sci., 309, 365
Gabici S., Casanova S., Aharonian F. A., Rowell G., 2010, in Proc. Société Francaise d'Astronomie et d'Astrophysique, p. 237 (arXiv:1007.4869v1)

Giuliani A. et al. (AGILE Collaboration), 2010, A&A, 516, L11
Goldsmith P. F., Langer W. D., 1999, ApJ, 517, 209
Gómez Y., Rodríguez L. F., Garay G., Moran J. M., 1991, ApJ, 377, 519
Goudis C., 1976, Ap&SS, 40, 91
Gusdorf A., Cabrit S., Flower D. R., Pineau Des Forêts G., 2008a, A&A, 482, 809
Gusdorf A., Pineau des Forêts G., Cabrit S., Flower D. R., 2008b, A&A, 490, 695
Harvey P. M., Forveille T., 1988, A&A, 197, L19
Hewitt J. W., Yusef-Zadeh F., 2009, ApJ, 694, L16
Hunter T. L., Brogan C. L., Indebetouw R., Cyganowski C. J., 2008, ApJ, 680, 1271
Inoue T., Yamazaki R., Inutsuka S., 2010, ApJ, 723, L108
Irvine W. M., Goldsmith P. F., Hjalmarson A., 1987, in Hollenbach D. J., Thronson H. A., Jr, eds, Chemical Abundances in Molecular Clouds. Interstellar Processes. Reidel, Deordrecht
Kaspi V. M., Lyne A. G., Manchester R. N., Johnston S., D'Amico N., Shemar S. L., 1993, ApJ, 409, L57
Kim K., Koo B., 2001, ApJ, 549, 979
Kim K., Koo B., 2003, ApJ, 596, 362
Kuchar T. A., Clark F. O., 1997, ApJ, 488, 224
Lefloch B., Cernicharo J., Pardo J. R., 2008, A&A, 489, 157
Li H., Chen Y., 2010, MNRAS, 409, L35
Linke R. A., Goldsmith P. F., 1980, ApJ, 235, 437
Liszt H. S., 2009, A&A, 508, 1331
Lockman F. J., 1989, ApJS, 71, 469
Lozinskaya T. A., 1981, Sov. Astron. Lett., 7, 17
Martin-Pintado J., de Vincente P., Rodríguez-Fernández N. J., Fuente A., Planesas P., 2000, A&A, 356, L5
Mizuno A., Fukui Y., 2004, in Clemens D., Shah R., Brainerd T., eds, ASP Conf. Proc. Vol. 317, Milky Way Surveys: The Structure and Evolution of our Galaxy. Astron. Soc. Pac., San Francisco, p. 59
Motogi K., Sorai K., Habe A., Honma M., Kobayashi H., Sato K., 2011, PASJ, 63, 31
Nicholas B., Rowell G., Burton M. G., Walsh A., Fukui Y., Kawamura A., Longmore S., Keto E., 2011, MNRAS, 411, 1367
Ohira Y., Murase K., Yamazaki R., 2011, MNRAS, 410, 1577
Reach W. T., Rho J., Jarrett T. H., 2005, ApJ, 618, 297
Rho J., Borkowski K. J., 2002, ApJ, 575, 201
Schilke P., Walmsley C. M., Pineau Des Forêts G., Flower D. R., 1997, A&A, 321, 293
Seta M. et al., 1998, ApJ, 505, 286
Sollins P. K. et al., 2004, ApJ, 616, L35
The CTA Consortium, 2010, preprint (arXiv:1008.3703v2)
Thompson M. A., Macdonald G. H., 1999, A&AS, 135, 531
Torres D. F., Romero G. E., Dame T. M., Combi J. A., Butt Y. M., 2003, Phys. Rep., 382, 303
Uchiyama Y., Blandford R. D., Funk S., Tajima H., Tanaka T., 2010, ApJ, 723, L122
Ueno M., Bamba A., Koyama K., 2003, in Kajita T., Asaoka Y., Kawachi A., Matsubara Y., Sasaki M., eds, Proc. 28th International Cosmic Ray Conference. p. 240
Urquhart J. S. et al., 2010, PASA, 27, 321
Velázquez P. F., Dubner G. M., Goss W. M., Green A. J., 2002, AJ, 124, 2145
Voronkov M. A., Caswell J. L., Ellingsen S. P., Sobolev A. M., 2010, MNRAS, 405, 2471
Wootten A., 1981, ApJ, 245, 105
Yamazaki R., Kohri K., Bamba A., Yoshida T., Tsuribe T., Takahara F., 2006, MNRAS, 371, 1975
Zhou S., Wu Y., Evans II N. J., Fuller G. A., Myers P. C., 1989, ApJ, 346, 168
Zijlstra A. A, Pottasch S. R, Engels D., Roelfsema P. R., Hekkert P. T. L., Umana G., 1990, MNRAS, 246, 217
Zinchenko I., Forsström V., Lapinov A., Mattila K., 1994, A&A, 288, 601

SUPPORTING INFORMATION

Additional Supporting Information may be found in the online version of this article:

Figure A1. Spectra for the line emission detected towards the IRAS 17589−2312 star formation core from mapping data.
Figure A2. Spectra of the SiO (1–0) $v = 1$, 2, 3 lines coming from the V5357 Sgr Variable Star of Mira Cet type.
Figure A3. Image showing the relationship between the diffuse and dense gas in the NE cloud.
Table A1. Line parameters from a Gaussian fit to the spectra, for lines detected in deep pointing observations.

Please note: Wiley-Blackwell are not responsible for the content or functionality of any supporting materials supplied by the authors. Any queries (other than missing material) should be directed to the corresponding author for the article.

This paper has been typeset from a TEX/LATEX file prepared by the author.